MMED-RAG: VERSATILE MULTIMODAL RAG SYSTEM FOR MEDICAL VISION LANGUAGE MODELS

Anonymous authors
Paper under double-blind review

ABSTRACT

Artificial Intelligence (AI) has demonstrated significant potential in healthcare, particularly in disease diagnosis and treatment planning. Recent progress in Medical Large Vision-Language Models (Med-LVLMs) has opened up new possibilities for interactive diagnostic tools. However, these models often suffer from factual hallucination, which can lead to incorrect diagnoses. Fine-tuning and retrieval-augmented generation (RAG) have emerged as methods to address these issues. However, the amount of high-quality data and distribution shifts between training data and deployment data limit the application of fine-tuning methods. Although RAG is lightweight and effective, existing RAG-based approaches are not sufficiently general to different medical domains and can potentially cause misalignment issues, both between modalities and between the model and the ground truth. In this paper, we propose a versatile multimodal RAG system, MMed-RAG, designed to enhance the factuality of Med-LVLMs. Our approach introduces a domain-aware retrieval mechanism, an adaptive retrieved contexts selection, and a provable RAG-based preference fine-tuning strategy. These innovations make the RAG process sufficiently general and reliable, significantly improving alignment when introducing retrieved contexts. Experimental results across five medical datasets (involving radiology, ophthalmology, pathology) on medical VQA and report generation demonstrate that MMed-RAG can achieve an average improvement of 43.8% in the factual accuracy of Med-LVLMs.

1 INTRODUCTION

Artificial Intelligence (AI) has already transformed healthcare and still has a lot of potential for further advancements (Tăuţan et al., 2021; Wang et al., 2019; Ye et al., 2021; Tu et al., 2024). Recently, Medical Large Vision-Language Models (Med-LVLMs) have shown great promise for advancing interactive and intelligent diagnosis (Li et al., 2023a; Moor et al., 2023; Zhang et al., 2023b; Wu et al., 2023b). Despite this potential (Li et al., 2023b; Wu et al., 2023a; Shi et al., 2024), current Med-LVLMs still face significant reliability issues, particularly their tendency to generate non-factual medical responses (Xia et al., 2024a; Royer et al., 2024; Chen et al., 2024a; Jiang et al., 2024), making them unreliable in critical medical applications. These factuality issues raise serious concerns when deploying such models in clinical settings, where even small diagnostic errors could lead to severe consequences for patient care.

Recently, researchers have begun to focus on improving the factuality of Med-LVLMs through various techniques, including fine-tuning (Li et al., 2023a; Moor et al., 2023; Thawkar et al., 2023; Zhang et al., 2023b; Chen et al., 2024b) and retrieval-augmented generation (RAG) (Xia et al., 2024b; He et al., 2024; Sun et al., 2024b). Fine-tuning is a direct method to improve model performance, but it faces several limitations in the medical field. First, there is a lack of sufficient high-quality labeled data for fine-tuning in the medical domain. Additionally, a distribution gap often exists between the training data and the real-world deployment data (Schrouff et al., 2022), leading to significantly worse model performance during deployment. Hence, RAG has emerged as a viable alternative by providing external references during the inference stage, enhancing the factuality of Med-LVLMs (Wu et al., 2023c; Gao et al., 2023). However, despite its advantages, current RAG implementations in Med-LVLMs have significant limitations. First, these methods tend to be *dataset-specific*, reducing their generalizability across various medical domains. Second, these models are still facing *misalignment issues* that lead to factuality problems. This misalignment may

arise from the impact of adding RAG on the original Med-LVLMs' *cross-modality alignment*, as well as on the *overall alignment* between the model and ground truth.

To address these challenges, we propose a versatile factual **M**ultimodal **Med**ical **RAG** system called **MMed-RAG**. Specifically, MMed-RAG first introduces a domain-aware retrieval mechanism, designed to handle different domains of medical images more effectively. Here, we design a domain identification module to adaptively select a corresponding retrieval model given the input medical image. Secondly, we include a adaptive calibration approach for selecting the number of retrieved contexts. Lastly, MMed-RAG incorporates RAG-based preference fine-tuning to enhance cross-modality alignment and overall alignment with ground truth. The preference pairs are designed to achieve two goals: first, to improve cross-modality alignment by encouraging the model to avoid generating responses without utilizing input medical images, even the responses are correct; second, to improve overall alignment by encouraging the model to understand retrieved contexts when unsure, while avoiding interference from irrelevant retrieved information.

The primary contribution of this paper is MMed-RAG, a versatile multimodal RAG system designed specifically for Med-LVLMs to generate more factual responses. Under mild assumptions, our theoretical analysis demonstrates that MMed-RAG mitigates both cross-modality misalignment and overall misalignment with ground truth. Furthermore, empirical results on five medical multimodal datasets, covering three medical image modalities (radiology, pathology, and ophthalmology), show that MMed-RAG significantly improves the factual accuracy of Med-LVLMs, achieving improvements of 18.5% and 69.1% on Medical VQA and report generation tasks, respectively, compared to the original Med-LVLM. These empirical findings further demonstrate the effectiveness of our proposed components and support the theoretical analysis in addressing misalignment issues.

2 Preliminaries

In this section, we will provide a brief overview of Med-LVLMs and preference optimization.

Medical Large Vision Language Models. Med-LVLMs bridge LLMs with medical visual modules, allowing the model to take medical image x_v and clinical query x_t as input x, and autoregressively predict the probability distribution of the next token. The text output is denoted as y.

Preference Optimization. Preference optimization has achieved remarkable results in LLM alignment. Give an input x, a language model policy π_θ can produce a conditional distribution $\pi_\theta(y \mid x)$ with y as the output text response. The recently popular DPO (Rafailov et al., 2023) utilizes preference data achieve objective alignment in LLMs. The preference data is defined as $\mathcal{D} = \{x^{(i)}, y_w^{(i)}, y_l^{(i)}\}_{i=1}^N$, where $y_w^{(i)}$ and $y_l^{(i)}$ represent preferred and dispreferred responses given an input prompt x. The probably of obtaining each preference pair is $p(y_w \succ y_l) = \sigma(r(x, y_w) - r(x, y_l))$, where $\sigma(\cdot)$ is the sigmoid function. In DPO, the optimization can be formulated as classification loss over the preference data as:

$$\mathcal{L}_{DPO}(\pi_\theta; \pi_{\text{ref}}) = -\mathbb{E}_{(x,y_w,y_l)\sim\mathcal{D}}\left[\log\sigma\left(\alpha\log\frac{\pi_\theta(y_w|x)}{\pi_{\text{ref}}(y_w|x)} - \alpha\log\frac{\pi_\theta(y_l|x)}{\pi_{\text{ref}}(y_l|x)}\right)\right]. \tag{1}$$

where π_θ represents the reference policy, which is the LLM fine-tuned through supervised learning.

3 MMed-RAG: A Versatile Medical RAG System

In this section, as illustrated in Figure 1, we will propose MMed-RAG, a versatile RAG system for improving the factuality of Med-LVLMs. Specifically, MMed-RAG consists of three complementary modules. First, we design a domain-aware retrieval mechanism to select the optimal retriever by feeding each given medical image to the domain identification module. Second, to select an optimal number of retrieved contexts and filter out low-quality information, MMed-RAG adopts a adaptive method by filtering out low-quality information using the similarity scores during the RAG phase. Lastly, we use a RAG-based preference fine-tuning approach to improve the cross-modality alignment and the overall alignment between groundtruth. We detail these steps as follows:

3.1 Domain-Aware Retrieval Mechanism

In MMed-RAG, we introduce a domain-aware retrieval mechanism to efficiently handle medical images from different sources (e.g., radiology, pathology, ophthalmology). Specifically, we first

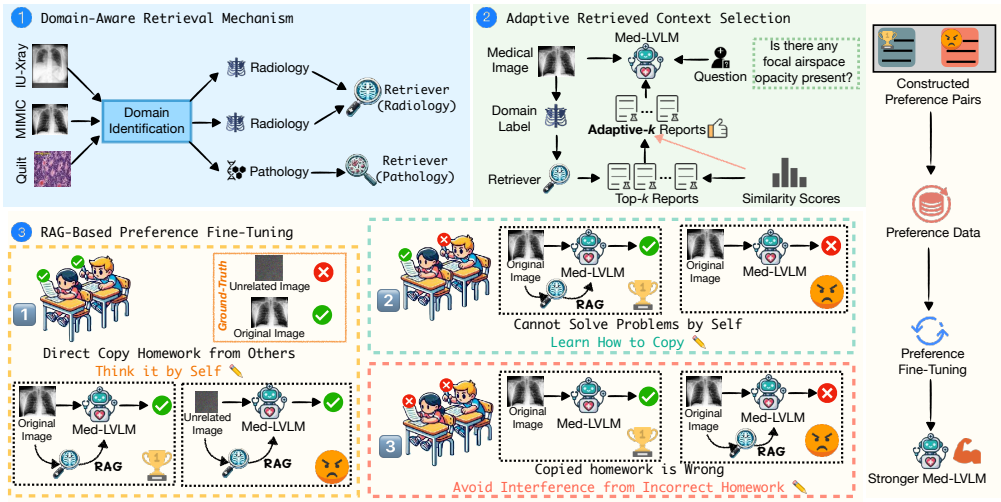

Figure 1: Overview of MMed-RAG, a versatile factual multimodal RAG system designed to enhance the reliability of Med-LVLMs. It introduces a domain-aware retrieval mechanism that effectively handles different domains of medical images by selecting suitable retrieval models. Additionally, it uses an adaptive context selection approach to determine the optimal number of retrieved contexts and employs preference fine-tuning to improve both cross-modality and overall alignment.

employ a domain identification module that assigns a domain label to each input medical image. To achieve this, we create a small dataset with medical images as inputs and their corresponding domain labels as outputs, using this dataset to fine-tune the BiomedCLIP model (Zhang et al., 2023a) to improve its domain awareness. Formally, for a given medical image x_v, we predict its domain $d = \mathcal{F}(x_v)$. Based on the assigned domain label d, the image x_v is fed into the corresponding multimodal retriever $\mathcal{R}_d(\cdot)$ for knowledge retrieval.

Here, each multimodal retriever $\mathcal{R}_d(\cdot)$ for each domain d is trained through contrastive learning (Radford et al., 2021). Specifically, the visual and textual information X_{img}, X_{txt} are processed by their corresponding encoders $\mathcal{E}_{img}(\cdot), \mathcal{E}_{txt}(\cdot)$ to generate textual and visual embeddings $V_{txt} = \mathcal{E}_{txt}(X_{txt}), V_{img} = \mathcal{E}_{img}(X_{img})$. Contrastive learning loss is then applied to maximize the similarity between text and image embeddings representing the same example, while minimizing the similarity between embeddings representing different examples, as defined below:

$$\mathcal{L} = \frac{\mathcal{L}_{img} + \mathcal{L}_{txt}}{2}, \text{where } \mathcal{L}_{img} = -\frac{1}{N}\sum_{i=1}^{N} \log \frac{\exp(S_{i,i})}{\sum_{j=1}^{N}\exp(S_{i,j})}, \mathcal{L}_{txt} = -\frac{1}{N}\sum_{i=1}^{N} \log \frac{\exp(S_{i,i})}{\sum_{j=1}^{N}\exp(S_{j,i})}, \tag{2}$$

where $S \in \mathbb{R}^{N\times N}$ represents the similarity matrix between image and text modalities, calculated as: $S = \frac{V_{img}}{|V_{img}|} \cdot (\frac{V_{txt}}{|V_{txt}|})^T$, where each element $S_{i,j}$ represents the similarity between the image representation of example i and the text representation of example j.

Finally, for the input image x_t, after feeding into the corresponding multimodal retriever $\mathcal{R}_d(\cdot)$, the multimodal retriever will retrieves the top-k most similar reports for the image. These retrieved reports $x_r = \mathcal{R}_d(x_v)$ are then provided to the Med-LVLM $\mathcal{M}(\cdot)$ as references to guide the generation.

3.2 Adaptive Retrieved Context Selection

Following the domain-aware retrieval mechanism, the next step is to determine the optimal amount of context to retrieve. Retrieving too much or too little information can result in hallucinations (Xia et al., 2024b). Current RAG methods applied to Med-LVLMs generally rely on empirical results or fixed values based on validation sets to select the optimal value of the number of retrieved contexts k (Xia et al., 2024b; He et al., 2024; Sun et al., 2024b). However, the distribution of similarity scores varies depending on the complexity of the image

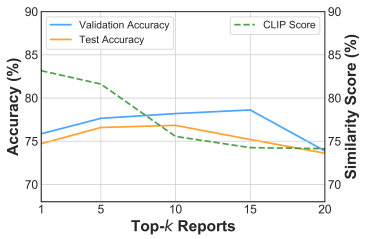

Figure 2: Relations between selected contexts and similarity score.

and its alignment with the textual information from the data source. These fixed-k methods do not guarantee optimal performance on target data, as they overlook the similarity scores generated during the retrieval process. To address this, we propose an adaptive method that dynamically selects k based on the similarity scores of the retrieved contexts. Specifically, during the domain-aware retrieval mechanism phase, the retrieved information is denoted as $x_r(k) = \mathcal{R}_d(x_v; k)$, where k represents the number of retrieved contexts, and the corresponding similarity scores are denoted as S_k. For simplicity, when there is no ambiguity, we will refer to $x_r(k)$ as x_r.

As illustrated in Figure 2, our method is based on a key observation: the similarity scores (CLIP score in this case) between retrieved contexts often exhibit a sharp decline after a certain number of results (nearly top-9 in this case). This suggests that lower-quality information can still be included among the top-k retrieved contexts when using a fixed-k strategy, especially in cases where the fixed value of k is too large. These lower-quality retrievals introduce noise and irrelevant information, which can significantly impair the model's ability to generate factual and coherent responses. To mitigate this issue, we draw inspiration from the Gap statistic method used in clustering (Tibshirani et al., 2001) and extend this concept to RAG for Med-LVLMs. Specifically, after retrieving the top-k contexts, we perform an additional round of k optimization by analyzing the similarity ratios between consecutive retrievals. These similarity ratios are denoted as $u_i = \log(S_i/S_{i+1})$ for $0 < i \leq k$, where S_i represents the similarity score of the i-th retrieved context. When u_i exceeds a predefined threshold γ, this indicates a substantial drop in relevance, suggesting that the remaining retrievals are less likely to contribute preferredly to the model's output. At this point i, we truncate k, effectively discarding the less relevant retrievals that follow. This adaptive truncation mechanism ensures that only the most relevant contexts are retained for generating the final response, reducing the risk of hallucination and improving the factual accuracy of the outputs.

Although the threshold γ is fixed, this approach provides a adaptive way to balance the bias and variance in retrieved contexts. By adapting to the characteristics of each input x_v, our method enhances the robustness of the retrieval process and ensures that the selection of k is tailored to the specific data at hand, thereby improving overall performance across diverse contexts and tasks.

3.3 RAG-BASED PREFERENCE FINE-TUNING

After context selection, MMed-RAG supplies Med-LVLM with reliable retrieved information as external knowledge to aid in generating factual responses. However, incorporating this retrieved knowledge may potentially disrupt the original alignment within the existing Med-LVLM, a concern we will elaborate on below:

Alignment Analysis. In the alignment analysis, we aim to explore how incorporating retrieved context impacts the original alignment in Med-LVLMs, focusing on two key aspects: (1) cross-modality alignment and (2) overall alignment with the ground truth. To evaluate cross-modality alignment, we conduct two tests on LLaVA-Med-1.5 (Li et al., 2023a) using the Harvard-FairVLMed (Luo et al., 2024) dataset. First, when replacing the original image with a highly noisy image associated with a different ground truth, the original model gives incorrect answers (the ground truth being the response for the original image). After incorporating RAG, where context is retrieved based on the original image, 55.08% of these cases return correct answers. This indicates that the model *directly references the retrieved knowledge* without considering the input image, highlighting significant *cross-modal misalignment issues*. Furthermore, 43.31% of the questions that were originally answered correctly are answered incorrectly after incorporating RAG, suggesting *interference from incorrect retrieval information*, which leads to *overall misalignment with the ground truth*.

To address cross-modality misalignment and the overall misalignment introduced by incorporating retrieved knowledge, as shown in Algorithm 1, we propose a RAG-based preference fine-tuning (RAG-PT) approach to fine-tune the target Med-LVLM $\mathcal{M}(\cdot)$. Specifically, RAG-PT constructs two types of preference pairs designed to mitigate both categories of misalignment.

Preference Pairs for Cross-Modality Alignment. We first construct preference pairs aimed at improving cross-modality alignment. In this dataset, we select samples from $\mathcal{D} = \{x_v^{(i)}, x_t^{(i)}, y^{(i)}\}_{i=1}^N$, where x_v, x_t, and y represent the input medical image, clinical query, and ground-truth answer, respectively. For simplicity, we omit the sample index (i) in the following sections. A model's correct response using retrieved knowledge, i.e., $\mathcal{M}(x_v, x_t + x_r) = y$, is considered a preferred response p_i, where x_r is the retrieved information. A dispreferred response n_i is selected from cases

Algorithm 1: Versatile Multimodal RAG System (MMed-RAG)

Input: $\mathcal{D} = \{x_v^{(i)}, x_t^{(i)}, y^{(i)}\}_{i=1}^N$: Dataset; π_θ: Parameters of the Med-LVLM; Med-LVLM: $\mathcal{M}(\cdot,\cdot)$; Domain Identification: $\mathcal{F}(\cdot)$; Retriever: $\mathcal{R}(\cdot)$; Noisy Function: $\mathcal{I}(\cdot)$.

Output: π_{ref}: Parameters of the reference model.

▷ ***Training Stage***
Initialize $\mathcal{D}_{cm}$ with an empty set
foreach $(x_v, x_t, y) \in \mathcal{D}$ **do**
  Generate retrieved contexts with an assigned domain label $x_r \leftarrow \mathcal{R}_{\mathcal{F}(x_v)}(x_v)$
  Generate the noisy image $x_v^* \leftarrow \mathcal{I}(x_v)$
  ▷ *Cross-Modality Alignment*
  if $\mathcal{M}(x_v, (x_t, x_r)) = y$ and $\mathcal{M}(x_v^*, (x_t, x_r)) = y$ **then**
    Select the preferred response $y_{w,o1} \leftarrow y$, dispreferred response $y_{l,o1} \leftarrow \mathcal{M}(x_v^*, (x_t, x_r))$
    Put $\{(x_v, x_t), y_{w,o1}, y_{l,o1}\}$ into $\mathcal{D}_{cm}$
  ▷ *Overall Alignment*
  Initialize $\mathcal{D}_{oa}^1$ and $\mathcal{D}_{oa}^2$ with empty set
  if $\mathcal{M}(x_v, (x_t, x_r)) = y$ and $\mathcal{M}(x_v, x_t) \neq y$ **then**
    Select the preferred response $y_{w,o2} \leftarrow y$, dispreferred response $y_{l,o2} \leftarrow \mathcal{M}(x_v, x_t)$
    Put $\{(x_v, x_t), y_{w,o2}, y_{l,o2}\}$ into $\mathcal{D}_{oa}^1$
  if $\mathcal{M}(x_v, x_t) = y$ and $\mathcal{M}(x_v, (x_t, x_r)) \neq y$ **then**
    Select the preferred response $y_{w,o3} \leftarrow y$, dispreferred response $y_{l,o3} \leftarrow \mathcal{M}(x_v, (x_t, x_r))$
    Put $\{(x_v, x_t), y_{w,o3}, y_{l,o3}\}$ into $\mathcal{D}_{oa}^2$
$\mathcal{D}_{pt} = \mathcal{D}_{cm} \cup \mathcal{D}_{oa}, \mathcal{D}_{oa} = \mathcal{D}_{oa}^1 \cup \mathcal{D}_{oa}^2$
foreach $((x_v, x_t), y_{w,o}, y_{l,o}) \in \mathcal{D}_{pt}$ **do**
  Compute the losses $\mathcal{L}_{pt}$ following equation 4 and update π_{ref}
▷ ***Inference Stage***
foreach test sample (x_v, x_t) **do**
  Select top-k retrieved contexts with an assigned domain label $x_r \leftarrow \mathcal{R}_{\mathcal{F}(x_v)}(x_v)$
  Get the predictions of the model w/ RAG-PT $p \leftarrow \mathcal{M}(x_v, (x_t, x_r))$

where the model makes a correct inference based on an unrelated image, i.e., $\mathcal{M}(x_v^*, x_t) \neq y$, but $\mathcal{M}(x_v^*, x_t + x_r) = y$, reflecting the model's reliance on the retrieved knowledge. The unrelated images x_v^* are generated through a two-step process: first, we use the retriever to select an image x_v' with the lowest similarity to the target image; then, we introduce diffusion noise into the selected unrelated image. We define the noise step as s, and the noised image at step s is expressed as:

$$x_v^* = \sqrt{\bar{\xi}_s} \cdot x_v' + \sqrt{1 - \bar{\xi}_s} \cdot \epsilon, \tag{3}$$

where $\bar{\xi}_s = \prod_{i=0}^{s} \xi_i$ and $\xi_s \in (0, 1)$ is a hyperparameter. The preference pairs constructed in this stage are denoted as $\mathcal{D}_{cm}$. By comparing the preferred and dispreferred responses in $\mathcal{D}_{cm}$, we encourage the model to prioritize the input medical image when generating responses.

Preference Pairs for Overall Alignment. Second, we construct preference pairs to improve overall alignment, focusing on enhancing the model's ability to effectively leverage retrieved knowledge when generating responses. The preference pairs in this stage are constructed from two subsets. The first subset, $\mathcal{D}_{oa}^1$, is designed to strengthen the model's comprehension and reasoning abilities regarding the retrieved knowledge. Preferred responses are selected where the model correctly answers based on both the original image and the retrieved information, i.e., $\mathcal{M}(x_v, x_t + x_r) = y$, while dispreferred responses represent cases where the model answers incorrectly based on the image without using retrieval, i.e., $\mathcal{M}(x_v, x_t) \neq y$. Comparing these preferred and dispreferred responses enhances the model's understanding of the retrieved information and improves the overall effectiveness of RAG. In the second subset, $\mathcal{D}_{oa}^2$, the goal is to mitigate interference from the retrieved knowledge. Preferred responses are selected where the model correctly answers based solely on the original image without using retrieved knowledge, i.e., $\mathcal{M}(x_v, x_t) = y$, while dispreferred responses occur when the model answers incorrectly using both the image and retrieved information, i.e., $\mathcal{M}(x_v, x_t + x_r) \neq y$. This helps the model learn when to rely on its internal knowledge versus retrieved knowledge. Finally, we combine the first and second subsets to form the second set of preference pairs, $\mathcal{D}_{oa} = \mathcal{D}_{oa}^1 \cup \mathcal{D}_{oa}^2$.

Finally, we merge the first and second preference set and denote the preference dataset as $\mathcal{D}_{pt} = \mathcal{D}_{cm} \cup \mathcal{D}_{oa} = \{x^{(i)}, y_{w,o}^{(i)}, y_{l,o}^{(i)}\}_{i=1}^N$, where $y_{w,o}^{(i)}$, $y_{l,o}^{(i)}$ are represented as preferred and dispreferred

responses, respectively. Based on the curated preferences, we fine-tune Med-LVLM using direct preference optimization (Rafailov et al., 2023) with the following loss:

$$\mathcal{L}_{pt} = -\mathbb{E}_{(x,y_{w,o},y_{l,o})\sim\mathcal{D}}\left[\log\sigma\left(\alpha\log\frac{\pi_\theta(y_{w,o}|x)}{\pi_o(y_{w,o}|x)} - \alpha\log\frac{\pi_\theta(y_{l,o}|x)}{\pi_o(y_{l,o}|x)}\right)\right]. \tag{4}$$

4 Theoretical Analysis

In this section, we provide a theoretical analysis of the model obtained from equation 4 and examine how the image input and retrieved context influences the model. Recall that x_v, y, x_t, x_r denotes input medical image, groundtruth answer, question, and retrieved information, respectively.

4.1 The Improvement on Cross-Modality Alignment

We first consider the loss for cross-modality alignment,

$$\mathcal{L}_{cm} = -\mathbb{E}_{(x,y_{w,o},y_{l,o})\sim\mathcal{D}_{cm}}\left[\log\sigma\left(\alpha\log\frac{\pi_\theta(y_{w,o}|x)}{\pi_o(y_{w,o}|x)} - \alpha\log\frac{\pi_\theta(y_{l,o}|x)}{\pi_o(y_{l,o}|x)}\right)\right]. \tag{5}$$

where $(x_w, y_{w,o}) \sim q_w(x_w, y_{w,o}|x_t, x_r)$ and $(x_l, y_{l,o}) \sim q_l(x_l, y_{l,o}|x_t, x_r)$ represent distributions of the preferred responses and dispreferred responses on $\mathcal{D}_{cm}$, respectively. Let x denote (x_v, x_r, x_t)

Definition 4.1 *Define the weight of x_v with respect to $\log\pi_\theta(y|x)$ as*

$$wt(x_v, \pi_\theta) := \mathbb{E}_{y\sim\pi_\theta(\cdot|x)}\left[\frac{\partial}{\partial x_v}\log\pi_\theta(y|x)\right]^2 \tag{6}$$

Definition 4.1 describes how $\log\pi_\theta(y|x)$ changes with respect to x_v, and the weight is always non-dispreferred. We demonstrate that this is a reasonable definition through Lemma 4.1.

Lemma 4.1 *For linear model $y = \theta_1 x_v + \theta_2 x_t + \epsilon$ such that $\epsilon \sim N(0,1)$, $wt(x_v, \pi_\theta) = \theta_1^2$*

Assumption 4.1 *Let $h(x, y)$, abbreviate as h, be*

$$h := \left[\sum_y \pi_o(y|x)\left(\frac{q_w(y|x)}{q_l(y|x)}\right)^{\frac{1}{\alpha}}\right]^{-1}\left(\frac{q_w(y|x)}{q_l(y|x)}\right)^{\frac{1}{\alpha}} \tag{7}$$

Assume that $wt(x_v, \pi_o) < c^2$, where

$$c = \sqrt{\left\|\sqrt{\pi_o(y|x)}\cdot\frac{\partial}{\partial x_v}h\right\|_2^2 + \int\left(\frac{\partial}{\partial x_v}h\right)^2\frac{\pi_o(y|x)}{h}dy} - \left\|\sqrt{\pi_o(y|x)}\cdot\frac{\partial}{\partial x_v}h\right\|_2 \tag{8}$$

Assumption 4.1 requires that x_v has a small weight in $\log\pi_o(y|x)$. A model $\pi_o(y|x)$ independent of x_v could satisfy Assumption 4.1. In this case, the reference model generates answers without using information from the image.

Theorem 4.1 *Suppose that Assumption 4.1 holds, cross-modality loss increase the weight of x_v.*

$$wt(x_v, \pi_\theta) > wt(x_v, \pi_o) \tag{9}$$

Theorem 4.1 indicates that when the weight of x_v is too small in the initial model $\pi_o(y|x)$, the cross-modality loss function adjusts the model to place greater emphasis on images, informed by the retrieved data. Intuitively, for any sample (x, y), generating unrelated images causes the policy to rely less on images. By using samples from this distribution as negative samples, the new model diverges from the initial model, increasing its reliance on images.

4.2 The Improvement on Overall Alignment

In this section, we analyze the improvement on overall alignment. Let $q_w^1(x_v, y_{w,o}|x_t, x_r)$ and $q_l^1(x_v, y_{l,o}|x_t)$ represent distributions of the preferred responses and dispreferred responses on $\mathcal{D}_{oa}^1$, respectively; $q_w^2(x_v, y_{w,o}|x_t)$ and $q_l^2(x_v, y_{l,o}|x_t, x_r)$ represent distributions of the preferred responses and dispreferred responses on $\mathcal{D}_{oa}^2$, respectively. Overall loss is defined by

$$\mathcal{L}_{oa} = -\mathbb{E}_{(x,y_{w,o},y_{l,o})\sim\mathcal{D}_{oa}}\left[\log\sigma\left(\alpha\log\frac{\pi_\theta(y_{w,o}|x)}{\pi_o(y_{w,o}|x)} - \alpha\log\frac{\pi_\theta(y_{l,o}|x)}{\pi_o(y_{l,o}|x)}\right)\right]. \tag{10}$$

Consider π as the generative distribution underlying $\mathcal{M}$, construction of $\mathcal{D}_{oa}^1$ and $\mathcal{D}_{oa}^2$ indicate that there is a significant gap between $\pi(y|x_v, x_t, x_r)$ and $\pi(y|x_v, x_t, \tilde{x}_r)$ for x_r generates true answer while $\tilde{x}_r$ generate a false one.

Assumption 4.2 *Assume that $\pi(y|x_x, x_r, x_t) : x \rightarrow y$ is L-lipschitz continuous on x_r for all (x_v, x_t, y) such that $|\pi(y|x_v, x_t, x_r) - \pi(y|x_v, x_t, \tilde{x}_r)| \leq L \cdot d_x(x_r, \tilde{x}_r)$, where d_x is any distance metric on the text space.*

Based on Assumption 4.2, $\tilde{x}_r$ can be viewed as being far from the meaningful retrieved information x_r, resulting in different weight in the model. Then, we claim in the following theorem that the overall loss in equation 10 can effectively leverage retrieved knowledge while training.

Assumption 4.3 *Let $h_1(x_v, x_t, x_r, y)$, abbreviate as h_1, be*

$$h_1 := \left[\sum_y \pi_o(y|x) \left(\frac{q_w^1(y|x_v, x_t, x_r) + q_w^2(y|x_v, x_t)}{q_l^1(y|x_v, x_t) + q_l^2(y|x_v, x_t, x_r)}\right)^{\frac{1}{\alpha}}\right]^{-1} \left(\frac{q_w^1(y|x_v, x_t, x_r) + q_w^2(y|x_v, x_t)}{q_l^1(y|x_v, x_t) + q_l^2(y|x_v, x_t, x_r)}\right)^{\frac{1}{\alpha}} \tag{11}$$

Assume that $wt(x_r, \pi_o) < c_1^2$ and $wt(\tilde{x}_r, \pi_o) > c_2^2$, where

$$\begin{aligned} c_1 &= \sqrt{\left\|\sqrt{\pi_o} \cdot \frac{\partial h_1}{\partial x_r}\right\|_2^2 + \int \left(\frac{\partial h_1}{\partial x_r}\right)^2 \frac{\pi_o}{h_1} dy} - \left\|\sqrt{\pi_o} \cdot \frac{\partial h_1}{\partial x_r}\right\|_2 \\ c_2 &= \sqrt{\left\|\sqrt{\pi_o} \cdot \frac{\partial h_1}{\partial \tilde{x}_r}\right\|_2^2 + \int \left(\frac{\partial h_1}{\partial \tilde{x}_r}\right)^2 \frac{\pi_o}{h_1} + \left(\frac{\partial \pi_o}{\partial \tilde{x}_r}\right)^2 \frac{h_1}{\pi_o} dy} + \left\|\sqrt{\pi_o} \cdot \frac{\partial h_1}{\partial \tilde{x}_r}\right\|_2 \end{aligned} \tag{12}$$

Theorem 4.2 *Suppose that Assumption 4.3 holds, then overall loss 10 increase the weight of x_r and decrease the weight of $\tilde{x}_r$.*

$$wt(x_r, \pi_\theta) > wt(x_r, \pi_o), \quad wt(\tilde{x}_r, \pi_\theta) < wt(\tilde{x}_r, \pi_o) \tag{13}$$

Theorem 4.2 suggests that the model tend to improve the overall alignment. When $\tilde{x}_r$ generates a false answer, the training procedure tends to reduce the reliance on $\tilde{x}_r$, resulting in a decrease in the weight assigned to $\tilde{x}_r$. Conversely, if x_r is helpful for generating the true answer, $\pi_\theta(y|x)$ tend to enhance its use of x_r.

5 EXPERIMENT

In this section, we evaluate the performance of MMed-RAG, aiming to answer the following questions: (1) Can MMed-RAG effectively improve the factuality of Med-LVLMs compared to decoding-based and RAG-based baselines? (2) How effective is each proposed component on performance? (3) What is the effect of preference data for different alignment goals? and (4) Does MMed-RAG actually improve cross-modality alignment and overall alignment?

5.1 EXPERIMENTAL SETUPS

Implementation Details. We use LLaVA-Med-1.5 7B (Li et al., 2023a) as the backbone model. During the preference fine-tuning process, we adapt LoRA fine-tuning (Hu et al., 2021). For the training of retriever, the vision encoder is a ResNet-50 (He et al., 2016), and the text encoder is a bio-BioClinicalBERT (Alsentzer et al., 2019). We use the AdamW optimizer with a learning rate of 10^{-3}, weight decay of 10^{-2} and a batch size of 32. The model is trained for 360 epochs. For more detailed information on training hyperparameters and training data, please see Appendix A.1.1.

Baseline Methods. We compare MMed-RAG with two types of LVLM hallucination mitigation methods that show promising results in natural image understanding. 1) Decoding-based methods, including Greedy Decoding, Beam Search (Sutskever et al., 2014), DoLa (Chuang et al., 2023), OPERA (Huang et al., 2023), VCD (Leng et al., 2023). These methods manipulate the logits of the model's output tokens to enhance factual accuracy. 2) Multimodal RAG-based methods, including MedDr (He et al., 2024), FactMM-RAG (Sun et al., 2024b), RULE (Xia et al., 2024b). Furthermore, we compare the performance with other open-source Med-LVLMs, including Med-Flamingo (Moor et al., 2023), MedVInT (Zhang et al., 2023b), RadFM (Wu et al., 2023b).

Table 1: Model performance (%) of different methods based on LLaVA-Med-1.5 on medical VQA task. Notably, we report the accuracy, F1 score and AUROC. The best results and second best results are highlighted in red and blue, respectively.

Models	Radiology						Ophthalmology			Pathology					
	IU-Xray			MIMIC-CXR			Harvard-FairVLMed			Quilt-1M			PMC-OA (Pathology)		
	Acc	F1	AUC	Acc	F1	AUC	Acc	F1	AUC	Acc	F1	AUC	Acc	F1	AUC
LLaVA-Med-1.5	75.47	64.04	67.46	75.79	80.49	68.84	63.03	74.11	63.05	62.80	72.90	60.03	59.28	71.98	54.19
+ Greedy	76.88	65.59	68.74	78.32	86.75	71.13	82.54	85.98	70.09	64.72	70.12	58.75	58.61	70.42	53.10
+ Beam Search	76.91	66.06	68.77	81.56	86.36	73.79	80.93	88.08	68.94	63.52	69.33	57.65	56.29	69.84	52.89
+ DoLa	78.00	66.75	72.19	81.35	85.73	72.73	76.87	85.53	67.10	63.47	69.10	57.58	57.71	70.27	52.95
+ OPERA	70.59	61.54	63.22	69.34	76.66	62.46	71.41	81.37	65.59	60.51	66.32	54.79	55.32	68.30	51.86
+ VCD	68.99	54.35	61.08	70.89	75.57	64.61	65.88	77.20	64.16	61.43	67.39	55.72	55.10	67.94	51.62
+ MedDr	83.33	67.80	77.15	55.16	56.18	58.47	70.17	80.72	64.15	68.15	73.23	67.01	59.97	69.19	57.01
+ FactMM-RAG	84.51	68.51	77.07	77.58	81.86	70.09	83.67	87.21	72.20	69.25	73.62	68.15	60.49	69.38	57.31
+ RULE	87.84	78.00	85.78	83.92	87.49	83.44	87.12	92.89	77.08	68.97	73.80	68.13	61.41	70.36	58.91
MMed-RAG	89.54	80.72	87.13	83.57	88.49	85.08	87.94	92.78	80.81	72.95	76.35	72.25	64.54	73.09	61.42

Table 2: Model performance (%) of different methods on report generation task. Notably, we report the average BLEU score, ROUGE-L, METEOR. For detailed BLEU score, see Appendix A.6.8.

Models	Radiology						Ophthalmology		
	IU-Xray			MIMIC-CXR			Harvard-FairVLMed		
	BLEU	ROUGE-L	METEOR	BLEU	ROUGE-L	METEOR	BLEU	ROUGE-L	METEOR
LLaVA-Med-1.5	9.64	12.26	8.21	12.11	13.05	11.16	18.11	11.36	10.75
+ Greedy	11.47	15.38	12.69	16.63	14.26	14.19	17.98	11.49	13.77
+ Beam Search	12.10	16.21	13.17	16.97	14.74	14.43	18.37	12.62	14.50
+ DoLa	11.79	15.82	12.72	17.11	14.89	14.81	18.26	12.51	14.51
+ OPERA	10.66	14.70	12.01	15.40	12.52	13.72	16.59	11.47	13.63
+ VCD	10.42	14.14	11.59	15.18	12.30	13.38	16.73	11.38	13.89
+ MedDr	12.37	16.45	13.50	18.59	15.72	16.77	19.82	13.72	15.40
+ FactMM-RAG	14.70	18.05	15.92	18.71	15.84	16.82	20.82	14.17	15.31
+ RULE	27.53	23.16	27.99	18.61	15.96	17.42	22.35	14.93	17.74
MMed-RAG	31.38	25.59	32.43	23.25	12.34	20.47	24.82	16.59	19.85

Evaluation Datasets. We utilize five medical vision-language datasets for medical VQA and report generation tasks, i.e., MIMIC-CXR (Johnson et al., 2019), IU-Xray (Demner-Fushman et al., 2016), Harvard-FairVLMed (Luo et al., 2024), PMC-OA (Lin et al., 2023a) (we only select the pathology part) and Quilt-1M (Ikezogwo et al., 2024). These datasets cover radiology, ophthalmology, and pathology. To construct the VQA benchmarks, following (Xia et al., 2024a), we generate question-answer pairs from medical reports using GPT-4 (OpenAI, 2023), with answers formatted as *yes* or *no*. Pathology images are excluded from the report generation task due to their brief and insufficient descriptions. The detailed dataset descriptions are provided in the Appendix A.2.

Evaluation Metrics. Following (Jing et al., 2017; Lin et al., 2023b), we use Accuracy, F1 Score and AUROC for evaluating medical VQA task, and BLEU Score (Papineni et al., 2002), ROUGE-L (Lin, 2004) and METEOR (Banerjee & Lavie, 2005) for evaluating report generation task.

5.2 Main Results

In this section, we provide a comprehensive comparison with various baseline methods and other open-source Med-LVLMs on medical VQA and report generation tasks.

Comparison with Baselines. We compare MMed-RAG with baseline methods on medical VQA and report generation tasks, with the results presented in Table 1 and Table 2, respectively. Overall, MMed-RAG outperforms all baselines across nearly all metrics and datasets. Specifically, MMed-RAG demonstrates a significant performance boost, improving by 18.5% and 69.1% over the original Med-LVLM in medical VQA and report generation tasks, respectively. When compared to baseline methods, MMed-RAG surpasses decoding-based approaches, achieving improvements of 11.5% and 44.2% in the two tasks. Furthermore, recent RAG-based methods show substantial improvements over earlier techniques, yet our approach still outperforms RAG-based baselines by 2.8% and 16.1% in the medical VQA and report generation tasks, respectively. This indicates that MMed-RAG effectively mitigates misalignment issues introduced by RAG. Notably, MMed-RAG achieves more pronounced gains in report generation, likely due to the higher complexity of the task and the greater influence of retrieved contexts in guiding open-ended generation.

Comparison with Other Med-LVLMs. To provide a comprehensive comparison, we evaluate MMed-RAG against other open-source Med-LVLMs to demonstrate the superiority of our approach. We assess the performance of these models across different medical image modalities, reporting the average results for medical VQA and report generation tasks in Table 3 (see Appendix A.6 for detailed results). Our findings show that MMed-RAG significantly outperforms Med-LVLMs pre-trained on large-scale datasets across various domains. This reinforces the generalizability and effectiveness of our approach across diverse image domains and medical multimodal tasks.

Table 3: Performance comparison with several Med-LVLMs. Rad: Radiology, Opt: Ophthalomology, Pat: Pathology.

Model	Rad	Opt	Pat
Med-Flamingo	27.42	22.50	29.11
MedVInT	33.17	29.40	25.33
RadFM	35.82	27.07	24.82
miniGPT-Med	36.66	25.28	23.16
MMed-RAG	**56.94**	**56.38**	**54.10**

5.3 Analysis

In this section, we provide a detailed analysis of each module's performance, along with a series of analytical experiments, to better understand the performance gains of MMed-RAG. Additionally, we demonstrate the compatibility of our method in Appendix A.6, including its application to generalist and domain-specific Med-LVLMs. In Appendix A.6.7 and A.6.4, we show the strong performance of our method on external validation datasets and in the environmental systems domain.

Ablation Studies. We conduct a series of ablation experiments to evaluate the impact of each component in MMed-RAG. The results for both medical VQA and report generation tasks on the IU-Xray and Harvard-FairVLMed datasets are summarized in Table 4. According to the results, we can see that: (1) The domain-aware retrieval mechanism (DR) significantly improves the factuality of Med-LVLM, with an average performance increase of 17.9% and 16.1% on the IU-Xray and FairVLMed datasets, respectively. Here, the retrieved knowledge aids the model in generating more factual responses. (2) Building on this, the introduction of adaptive retrieval context selection (RCS) further filters out unreliable retrieved contexts, yielding an additional performance boost of 19.3% and 6.3% on the IU-Xray and FairVLMed datasets. (3) The inclusion of RAG-based preference fine-tuning (RAG-PT) enhances the model's understanding of the retrieved knowledge, leading to substantial performance gains of 37.1% and 16.9% on the respective datasets. This demonstrates that RAG-PT effectively addresses misalignment issues.

Table 4: Ablation results on two datasets covering different domains. RG: report generation, FairVLMed: Harvard-FairVLMed.

Model	IU-Xray		FairVLMed	
	VQA	RG	VQA	RG
LLaVA-Med-1.5	68.99	10.04	66.63	13.41
+DR	77.12	13.23	72.69	15.89
+RCS	79.56	17.92	75.74	17.22
+RAG-PT (Ours)	**85.80**	**29.80**	**87.18**	**20.42**

Impact of the Preference Data in RAG-PT. To better understand how RAG-PT mitigates the misalignment issue and improves performance, we conducted a detailed study on the training preference data composition of RAG-PT. As described in Section 3.3, the RAG-PT data is designed to address both cross-modality alignment and overall alignment objectives, with the latter focusing on enhanced understanding of retrieved knowledge and minimizing retrieval interference. The detailed experimental results in Table 5 demonstrate that the preference data tailored for different alignment objectives positively impacts the model's performance, showing the effectiveness of RAG-PT. We present additional ablation results on preference data in Appendix A.6.6.

Table 5: Performance using RAG-PT based on subsets of preference data.

Model	IU-Xray		FairVLMed	
	VQA	RG	VQA	RG
LLaVA-Med-1.5	68.99	10.04	66.63	13.41
+RAG-PT 1	80.19	19.38	79.42	18.37
+RAG-PT 2	80.27	**20.16**	79.35	18.66
+RAG-PT 3	**81.30**	19.43	**80.07**	**18.92**

How Effective is MMed-RAG in Mitigating Misalignment Issues? To gain a more intuitive understanding of the effectiveness of MMed-RAG in addressing misalignment issues: 1) we calculate the proportion of errors caused by RAG and compare it to the proportion after incorporating MMed-RAG. 2) We visualize the attention maps of image and text tokens with and without RAG-PT. First, as mentioned in Section 3.3, the model may directly copy reference information, referred to as Copy-Reference (CR) rate. After applying MMed-RAG, as shown in Figure 3, the CR rate drops to 28.19%. Additionally, the proportion of errors affected by RAG interference, referred to as Over-Reliance (OR) rate, which is initially 43.31%, decreased to 8.38% after incorporating MMed-RAG. Furthermore, as shown in Figure 4, the original Med-LVLM tends to rely more heavily on text while

ignoring visual information. When retrieval information is introduced, the original Med-LVLM focused more on the retrieved answers, even if the content is incorrect. After RAG-PT, the model significantly increases its attention to visual information and reduces the interference of RAG, thus better aligning the model's knowledge with the fundamental facts.

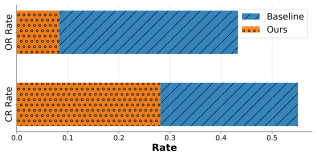

Figure 3: Alignment analysis with and without RAG. OR: Over-Reliance; CR: Copy-Reference.

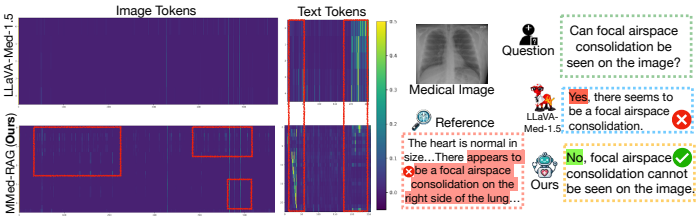

Figure 4: Visualization of attention map. The red box region is labeled with the attentions that can be enhanced by MMed-RAG.

6 Related Work

Factuality in Med-LVLMs. The rapid advancements in Large Vision-Language Models (LVLMs) (Liu et al., 2024a;b) are beginning to influence the field of medical image analysis. Several Med-LVLMs (Li et al., 2023a; Moor et al., 2023; Zhang et al., 2023b; Wu et al., 2023b), have emerged, showing remarkable performance across different medical imaging modalities. Despite these advances, Med-LVLMs continue to present notable factual hallucination (Xia et al., 2024a; Royer et al., 2024), generating textual outputs that contradict medical visual information. This raises concerns about potential misdiagnoses or overlooked conditions. Recently, benchmarks have been developed to assess the accuracy of Med-LVLMs in tasks such as visual question answering (VQA) and report generation (Xia et al., 2024a; Royer et al., 2024). However, research aimed at enhancing the factual accuracy of Med-LVLMs remains relatively unexplored.

Retrieval Augmented Generation in Med-LVLMs. Retrieval-Augmented Generation (RAG) has proven to be a powerful technique for enhancing factual accuracy in language modeling (Gao et al., 2023; Wu et al., 2023c; Chen et al., 2024c; Qu et al., 2024; Sun et al., 2024a). In the biomedical domain, RAG leverages external knowledge to guide the generation of Med-LVLMs, offering clear advantages in tasks such as medical VQA and report generation (Yuan et al., 2023; Kumar & Marttinen, 2024; Tao et al., 2024; He et al., 2024; Sun et al., 2024b). However, these works mainly focus on enhancing the relevance of the retrieved contexts without considering the model's understanding of retrieved knowledge. There are several recent work on RAG fine-tuning in LLMs. DPA-RAG (Dong et al., 2024) addresses the alignment issues between the external reranker and the internal LLM through supervised fine-tuning. Then RAG-DDR (Li et al., 2024b) leverages a rolling method to generate perturbed responses, further mitigating conflicts between parameter memory and external knowledge. In the biomedical domain, RULE (Xia et al., 2024b) is proposed to use preference fine-tuning to reduce the model's over-reliance on retrieved contexts. However, it still overlooks misalignment issues caused by RAG, as well as the generalizability of the retriever given the diverse domains of input images. In response, we propose MMed-RAG to mitigate these risks, enhancing the factuality of Med-LVLMs by addressing these overlooked factors. This can lead to a better cross-modality and overall alignment to enhance the understanding of retrieved knowledge and visual information, ensuring more consistent and reliable performance across tasks.

7 Conclusion

This paper introduces MMed-RAG, a versatile multimodal RAG system designed to address the critical issue of factual hallucination in Med-LVLMs. MMed-RAG employs a domain-aware retrieval mechanism, adaptive calibration for selecting the optimal number of retrieved contexts, and RAG-based preference fine-tuning to improve both cross-modality alignment and overall alignment with the ground truth. These enhancements significantly boost the factual accuracy of Med-LVLMs. Experimental results demonstrate MMed-RAG' effectiveness in enhancing factual accuracy across various imaging domains, underscoring its potential for reliable use in healthcare. Our findings underscore the importance of incorporating robust multimodal RAG mechanism to ensure that Med-LVLMs can serve as dependable tools in clinical settings.

ETHICS STATEMENT

This paper presents a novel RAG-based approach to enhancing the factuality of Med-LVLMs. We have followed best practices in data collection, model design, and evaluation, ensuring adherence to privacy and ethical standards. All datasets used are sourced from publicly available medical datasets or collected with appropriate ethical considerations, including patient data anonymization. We adhere to principles of research integrity and transparency, and comply with all relevant regulations. We hope that our research will contribute to safer, more reliable AI-assisted medical tools and advance healthcare technology responsibly.

REPRODUCIBILITY STATEMENT

We have taken significant steps to ensure that our work is reproducible. All details regarding our proposed multimodal RAG system, including the domain-aware retrieval mechanism, adaptive retrieved context selection, and RAG-based preference fine-tuning strategy, are described comprehensively in Section 3. We provide the hyperparameter settings and experimental configurations used in our evaluations in Section 5.1 and Appendix A.1.2. Additionally, we have included detailed pseudocode for the proposed algorithms in Algorithm 1 and an in-depth explanation of the data processing steps for each medical dataset used in Appendix A.1.1 and Appendix A.2.

REFERENCES

Asma Alkhaldi, Raneem Alnajim, Layan Alabdullatef, Rawan Alyahya, Jun Chen, Deyao Zhu, Ahmed Alsinan, and Mohamed Elhoseiny. Minigpt-med: Large language model as a general interface for radiology diagnosis. arXiv preprint arXiv:2407.04106, 2024.

Emily Alsentzer, John R Murphy, Willie Boag, Wei-Hung Weng, Di Jin, Tristan Naumann, and Matthew McDermott. Publicly available clinical bert embeddings. arXiv preprint arXiv:1904.03323, 2019.

Jinze Bai, Shuai Bai, Shusheng Yang, Shijie Wang, Sinan Tan, Peng Wang, Junyang Lin, Chang Zhou, and Jingren Zhou. Qwen-vl: A versatile vision-language model for understanding, localization, text reading, and beyond. 2023.

Satanjeev Banerjee and Alon Lavie. Meteor: An automatic metric for mt evaluation with improved correlation with human judgments. In Proceedings of the acl workshop on intrinsic and extrinsic evaluation measures for machine translation and/or summarization, pp. 65–72, 2005.

Jiawei Chen, Dingkang Yang, Tong Wu, Yue Jiang, Xiaolu Hou, Mingcheng Li, Shunli Wang, Dongling Xiao, Ke Li, and Lihua Zhang. Detecting and evaluating medical hallucinations in large vision language models. arXiv preprint arXiv:2406.10185, 2024a.

Junying Chen, Ruyi Ouyang, Anningzhe Gao, Shunian Chen, Guiming Hardy Chen, Xidong Wang, Ruifei Zhang, Zhenyang Cai, Ke Ji, Guangjun Yu, et al. Huatuogpt-vision, towards injecting medical visual knowledge into multimodal llms at scale. arXiv preprint arXiv:2406.19280, 2024b.

Zhanpeng Chen, Chengjin Xu, Yiyan Qi, and Jian Guo. Mllm is a strong reranker: Advancing multimodal retrieval-augmented generation via knowledge-enhanced reranking and noise-injected training. arXiv preprint arXiv:2407.21439, 2024c.

Zhe Chen, Weiyun Wang, Hao Tian, Shenglong Ye, Zhangwei Gao, Erfei Cui, Wenwen Tong, Kongzhi Hu, Jiapeng Luo, Zheng Ma, et al. How far are we to gpt-4v? closing the gap to commercial multimodal models with open-source suites. arXiv preprint arXiv:2404.16821, 2024d.

Zixiang Chen, Yihe Deng, Huizhuo Yuan, Kaixuan Ji, and Quanquan Gu. Self-play fine-tuning converts weak language models to strong language models, 2024e. URL https://arxiv.org/abs/2401.01335.

Clément Christophe, Praveen K Kanithi, Tathagata Raha, Shadab Khan, and Marco AF Pimentel. Med42-v2: A suite of clinical llms. arXiv preprint arXiv:2408.06142, 2024.

Yung-Sung Chuang, Yujia Xie, Hongyin Luo, Yoon Kim, James Glass, and Pengcheng He. Dola: Decoding by contrasting layers improves factuality in large language models. arXiv preprint arXiv:2309.03883, 2023.

Dina Demner-Fushman, Marc D Kohli, Marc B Rosenman, Sonya E Shooshan, Laritza Rodriguez, Sameer Antani, George R Thoma, and Clement J McDonald. Preparing a collection of radiology examinations for distribution and retrieval. Journal of the American Medical Informatics Association, 23(2):304–310, 2016.

Guanting Dong, Yutao Zhu, Chenghao Zhang, Zechen Wang, Zhicheng Dou, and Ji-Rong Wen. Understand what llm needs: Dual preference alignment for retrieval-augmented generation. arXiv preprint arXiv:2406.18676, 2024.

Yunfan Gao, Yun Xiong, Xinyu Gao, Kangxiang Jia, Jinliu Pan, Yuxi Bi, Yi Dai, Jiawei Sun, and Haofen Wang. Retrieval-augmented generation for large language models: A survey. arXiv preprint arXiv:2312.10997, 2023.

Pierre Gravel, Gilles Beaudoin, and Jacques A De Guise. A method for modeling noise in medical images. IEEE Transactions on medical imaging, 23(10):1221–1232, 2004.

Kaiming He, Xiangyu Zhang, Shaoqing Ren, and Jian Sun. Deep residual learning for image recognition. In Proceedings of the IEEE Conference on Computer Vision and Pattern Recognition, pp. 770–778, 2016.

Sunan He, Yuxiang Nie, Zhixuan Chen, Zhiyuan Cai, Hongmei Wang, Shu Yang, and Hao Chen. Meddr: Diagnosis-guided bootstrapping for large-scale medical vision-language learning. arXiv preprint arXiv:2404.15127, 2024.

Robbie Holland, Thomas RP Taylor, Christopher Holmes, Sophie Riedl, Julia Mai, Maria Patsiamanidi, Dimitra Mitsopoulou, Paul Hager, Philip Müller, Hendrik PN Scholl, et al. Specialist vision-language models for clinical ophthalmology. arXiv preprint arXiv:2407.08410, 2024.

Edward J Hu, Yelong Shen, Phillip Wallis, Zeyuan Allen-Zhu, Yuanzhi Li, Shean Wang, Lu Wang, and Weizhu Chen. Lora: Low-rank adaptation of large language models. arXiv preprint arXiv:2106.09685, 2021.

Qidong Huang, Xiaoyi Dong, Pan Zhang, Bin Wang, Conghui He, Jiaqi Wang, Dahua Lin, Weiming Zhang, and Nenghai Yu. Opera: Alleviating hallucination in multi-modal large language models via over-trust penalty and retrospection-allocation. arXiv preprint arXiv:2311.17911, 2023.

Wisdom Ikezogwo, Saygin Seyfioglu, Fatemeh Ghezloo, Dylan Geva, Fatwir Sheikh Mohammed, Pavan Kumar Anand, Ranjay Krishna, and Linda Shapiro. Quilt-1m: One million image-text pairs for histopathology. Advances in neural information processing systems, 36, 2024.

Yue Jiang, Jiawei Chen, Dingkang Yang, Mingcheng Li, Shunli Wang, Tong Wu, Ke Li, and Lihua Zhang. Medthink: Inducing medical large-scale visual language models to hallucinate less by thinking more. arXiv preprint arXiv:2406.11451, 2024.

Baoyu Jing, Pengtao Xie, and Eric Xing. On the automatic generation of medical imaging reports. arXiv preprint arXiv:1711.08195, 2017.

Alistair EW Johnson, Tom J Pollard, Nathaniel R Greenbaum, Matthew P Lungren, Chih-ying Deng, Yifan Peng, Zhiyong Lu, Roger G Mark, Seth J Berkowitz, and Steven Horng. Mimic-cxr-jpg, a large publicly available database of labeled chest radiographs. arXiv preprint arXiv:1901.07042, 2019.

Yogesh Kumar and Pekka Marttinen. Improving medical multi-modal contrastive learning with expert annotations. arXiv preprint arXiv:2403.10153, 2024.

Sicong Leng, Hang Zhang, Guanzheng Chen, Xin Li, Shijian Lu, Chunyan Miao, and Lidong Bing. Mitigating object hallucinations in large vision-language models through visual contrastive decoding. arXiv preprint arXiv:2311.16922, 2023.

Chunyuan Li, Cliff Wong, Sheng Zhang, Naoto Usuyama, Haotian Liu, Jianwei Yang, Tristan Naumann, Hoifung Poon, and Jianfeng Gao. Llava-med: Training a large language-and-vision assistant for biomedicine in one day. In Thirty-seventh Conference on Neural Information Processing Systems Datasets and Benchmarks Track, 2023a.

Haoran Li, Junqi Liu, Zexian Wang, Shiyuan Luo, Xiaowei Jia, and Huaxiu Yao. Lite: Modeling environmental ecosystems with multimodal large language models. arXiv preprint arXiv:2404.01165, 2024a.

Xinze Li, Sen Mei, Zhenghao Liu, Yukun Yan, Shuo Wang, Shi Yu, Zheni Zeng, Hao Chen, Ge Yu, Zhiyuan Liu, et al. Rag-ddr: Optimizing retrieval-augmented generation using differentiable data rewards. arXiv preprint arXiv:2410.13509, 2024b.

Yingshu Li, Yunyi Liu, Zhanyu Wang, Xinyu Liang, Lingqiao Liu, Lei Wang, Leyang Cui, Zhaopeng Tu, Longyue Wang, and Luping Zhou. A comprehensive study of gpt-4v's multimodal capabilities in medical imaging. arXiv preprint arXiv:2310.20381, 2023b.

Chin-Yew Lin. Rouge: A package for automatic evaluation of summaries. In Text summarization branches out, pp. 74–81, 2004.

Weixiong Lin, Ziheng Zhao, Xiaoman Zhang, Chaoyi Wu, Ya Zhang, Yanfeng Wang, and Weidi Xie. Pmc-clip: Contrastive language-image pre-training using biomedical documents. In International Conference on Medical Image Computing and Computer-Assisted Intervention, pp. 525–536. Springer, 2023a.

Zhihong Lin, Donghao Zhang, Qingyi Tao, Danli Shi, Gholamreza Haffari, Qi Wu, Mingguang He, and Zongyuan Ge. Medical visual question answering: A survey. Artificial Intelligence in Medicine, 143:102611, 2023b.

Haotian Liu, Chunyuan Li, Yuheng Li, and Yong Jae Lee. Improved baselines with visual instruction tuning. In Proceedings of the IEEE/CVF Conference on Computer Vision and Pattern Recognition, pp. 26296–26306, 2024a.

Haotian Liu, Chunyuan Li, Qingyang Wu, and Yong Jae Lee. Visual instruction tuning. Advances in neural information processing systems, 36, 2024b.

Yan Luo, Min Shi, Muhammad Osama Khan, Muhammad Muneeb Afzal, Hao Huang, Shuaihang Yuan, Yu Tian, Luo Song, Ava Kouhana, Tobias Elze, et al. Fairclip: Harnessing fairness in vision-language learning. arXiv preprint arXiv:2403.19949, 2024.

Fanqing Meng, Jin Wang, Chuanhao Li, Quanfeng Lu, Hao Tian, Jiaqi Liao, Xizhou Zhu, Jifeng Dai, Yu Qiao, Ping Luo, et al. Mmiu: Multimodal multi-image understanding for evaluating large vision-language models. arXiv preprint arXiv:2408.02718, 2024.

Michael Moor, Qian Huang, Shirley Wu, Michihiro Yasunaga, Yash Dalmia, Jure Leskovec, Cyril Zakka, Eduardo Pontes Reis, and Pranav Rajpurkar. Med-flamingo: a multimodal medical few-shot learner. In Machine Learning for Health (ML4H), pp. 353–367. PMLR, 2023.

OpenAI. Gpt-4 technical report, 2023. https://arxiv.org/abs/2303.08774.

Kishore Papineni, Salim Roukos, Todd Ward, and Wei-Jing Zhu. Bleu: a method for automatic evaluation of machine translation. In Proceedings of the 40th annual meeting of the Association for Computational Linguistics, pp. 311–318, 2002.

Xiaoye Qu, Qiyuan Chen, Wei Wei, Jishuo Sun, and Jianfeng Dong. Alleviating hallucination in large vision-language models with active retrieval augmentation. arXiv preprint arXiv:2408.00555, 2024.

Alec Radford, Jong Wook Kim, Chris Hallacy, Aditya Ramesh, Gabriel Goh, Sandhini Agarwal, Girish Sastry, Amanda Askell, Pamela Mishkin, Jack Clark, Gretchen Krueger, and Ilya Sutskever. Learning transferable visual models from natural language supervision, 2021.

Rafael Rafailov, Archit Sharma, Eric Mitchell, Christopher D Manning, Stefano Ermon, and Chelsea Finn. Direct preference optimization: Your language model is secretly a reward model. In Thirty-seventh Conference on Neural Information Processing Systems, 2023.

Machel Reid, Nikolay Savinov, Denis Teplyashin, Dmitry Lepikhin, Timothy Lillicrap, Jean-baptiste Alayrac, Radu Soricut, Angeliki Lazaridou, Orhan Firat, Julian Schrittwieser, et al. Gemini 1.5: Unlocking multimodal understanding across millions of tokens of context. arXiv preprint arXiv:2403.05530, 2024.

Carlos Riquelme, Joan Puigcerver, Basil Mustafa, Maxim Neumann, Rodolphe Jenatton, André Susano Pinto, Daniel Keysers, and Neil Houlsby. Scaling vision with sparse mixture of experts. Advances in Neural Information Processing Systems, 34:8583–8595, 2021.

Corentin Royer, Bjoern Menze, and Anjany Sekuboyina. Multimedeval: A benchmark and a toolkit for evaluating medical vision-language models. arXiv preprint arXiv:2402.09262, 2024.

Ma Guadalupe Sanchez, Ma Guadalupe Sánchez, Vicente Vidal, Gumersindo Verdu, Gumersindo Verdú, Patricia Mayo, and Francisco Rodenas. Medical image restoration with different types of noise. In 2012 Annual International Conference of the IEEE Engineering in Medicine and Biology Society, pp. 4382–4385. IEEE, 2012.

Jessica Schrouff, Natalie Harris, Sanmi Koyejo, Ibrahim M Alabdulmohsin, Eva Schnider, Krista Opsahl-Ong, Alexander Brown, Subhrajit Roy, Diana Mincu, Christina Chen, et al. Diagnosing failures of fairness transfer across distribution shift in real-world medical settings. Advances in Neural Information Processing Systems, 35:19304–19318, 2022.

Mehmet Saygin Seyfioglu, Wisdom O Ikezogwo, Fatemeh Ghezloo, Ranjay Krishna, and Linda Shapiro. Quilt-llava: Visual instruction tuning by extracting localized narratives from open-source histopathology videos. In Proceedings of the IEEE/CVF Conference on Computer Vision and Pattern Recognition, pp. 13183–13192, 2024.

Noam Shazeer, Azalia Mirhoseini, Krzysztof Maziarz, Andy Davis, Quoc Le, Geoffrey Hinton, and Jeff Dean. Outrageously large neural networks: The sparsely-gated mixture-of-experts layer. arXiv preprint arXiv:1701.06538, 2017.

Congzhen Shi, Ryan Rezai, Jiaxi Yang, Qi Dou, and Xiaoxiao Li. A survey on trustworthiness in foundation models for medical image analysis. arXiv preprint arXiv:2407.15851, 2024.

Jiashuo Sun, Jihai Zhang, Yucheng Zhou, Zhaochen Su, Xiaoye Qu, and Yu Cheng. Surf: Teaching large vision-language models to selectively utilize retrieved information. arXiv preprint arXiv:2409.14083, 2024a.

Liwen Sun, James Zhao, Megan Han, and Chenyan Xiong. Fact-aware multimodal retrieval augmentation for accurate medical radiology report generation. arXiv preprint arXiv:2407.15268, 2024b.

Ilya Sutskever, Oriol Vinyals, and Quoc V Le. Sequence to sequence learning with neural networks. In Advances in neural information processing systems, pp. 3104–3112, 2014.

Yitian Tao, Liyan Ma, Jing Yu, and Han Zhang. Memory-based cross-modal semantic alignment network for radiology report generation. IEEE Journal of Biomedical and Health Informatics, 2024.

Alexandra-Maria Tăuţan, Bogdan Ionescu, and Emiliano Santarnecchi. Artificial intelligence in neurodegenerative diseases: A review of available tools with a focus on machine learning techniques. Artificial Intelligence in Medicine, 117:102081, 2021.

Omkar Thawkar, Abdelrahman Shaker, Sahal Shaji Mullappilly, Hisham Cholakkal, Rao Muhammad Anwer, Salman Khan, Jorma Laaksonen, and Fahad Shahbaz Khan. Xraygpt: Chest radiographs summarization using medical vision-language models. arXiv preprint arXiv:2306.07971, 2023.

Robert Tibshirani, Guenther Walther, and Trevor Hastie. Estimating the number of clusters in a data set via the gap statistic. Journal of the Royal Statistical Society: Series B (Statistical Methodology), 63(2):411–423, 2001.

Hugo Touvron, Louis Martin, Kevin Stone, Peter Albert, Amjad Almahairi, Yasmine Babaei, Nikolay Bashlykov, Soumya Batra, Prajjwal Bhargava, and Shruti Bhosale. Llama 2: Open foundation and fine-tuned chat models. arXiv preprint arXiv:2307.09288, 2023.

Tao Tu, Shekoofeh Azizi, Danny Driess, Mike Schaekermann, Mohamed Amin, Pi-Chuan Chang, Andrew Carroll, Charles Lau, Ryutaro Tanno, Ira Ktena, et al. Towards generalist biomedical ai. NEJM AI, 1(3):AIoa2300138, 2024.

Chunhao Wang, Xiaofeng Zhu, Julian C Hong, and Dandan Zheng. Artificial intelligence in radiotherapy treatment planning: present and future. Technology in cancer research & treatment, 18: 1533033819873922, 2019.

Xiyao Wang, Yuhang Zhou, Xiaoyu Liu, Hongjin Lu, Yuancheng Xu, Feihong He, Jaehong Yoon, Taixi Lu, Gedas Bertasius, Mohit Bansal, et al. Mementos: A comprehensive benchmark for multimodal large language model reasoning over image sequences. arXiv preprint arXiv:2401.10529, 2024.

Zhepei Wei, Wei-Lin Chen, and Yu Meng. Instructrag: Instructing retrieval-augmented generation with explicit denoising. arXiv preprint arXiv:2406.13629, 2024.

Chaoyi Wu, Jiayu Lei, Qiaoyu Zheng, Weike Zhao, Weixiong Lin, Xiaoman Zhang, Xiao Zhou, Ziheng Zhao, Ya Zhang, Yanfeng Wang, et al. Can gpt-4v (ision) serve medical applications? case studies on gpt-4v for multimodal medical diagnosis. arXiv preprint arXiv:2310.09909, 2023a.

Chaoyi Wu, Xiaoman Zhang, Ya Zhang, Yanfeng Wang, and Weidi Xie. Towards generalist foundation model for radiology. arXiv preprint arXiv:2308.02463, 2023b.

Yuanhao Wu, Juno Zhu, Siliang Xu, Kashun Shum, Cheng Niu, Randy Zhong, Juntong Song, and Tong Zhang. Ragtruth: A hallucination corpus for developing trustworthy retrieval-augmented language models. arXiv preprint arXiv:2401.00396, 2023c.

Peng Xia, Ze Chen, Juanxi Tian, Yangrui Gong, Ruibo Hou, Yue Xu, Zhenbang Wu, Zhiyuan Fan, Yiyang Zhou, Kangyu Zhu, et al. Cares: A comprehensive benchmark of trustworthiness in medical vision language models. arXiv preprint arXiv:2406.06007, 2024a.

Peng Xia, Kangyu Zhu, Haoran Li, Hongtu Zhu, Yun Li, Gang Li, Linjun Zhang, and Huaxiu Yao. Rule: Reliable multimodal rag for factuality in medical vision language models. arXiv preprint arXiv:2407.05131, 2024b.

Qing Ye, Chang-Yu Hsieh, Ziyi Yang, Yu Kang, Jiming Chen, Dongsheng Cao, Shibo He, and Tingjun Hou. A unified drug–target interaction prediction framework based on knowledge graph and recommendation system. Nature communications, 12(1):6775, 2021.

Zheng Yuan, Qiao Jin, Chuanqi Tan, Zhengyun Zhao, Hongyi Yuan, Fei Huang, and Songfang Huang. Ramm: Retrieval-augmented biomedical visual question answering with multi-modal pre-training. In Proceedings of the 31st ACM International Conference on Multimedia, pp. 547–556, 2023.

Jihai Zhang, Xiaoye Qu, Tong Zhu, and Yu Cheng. Clip-moe: Towards building mixture of experts for clip with diversified multiplet upcycling. arXiv preprint arXiv:2409.19291, 2024.

Sheng Zhang, Yanbo Xu, Naoto Usuyama, Hanwen Xu, Jaspreet Bagga, Robert Tinn, Sam Preston, Rajesh Rao, Mu Wei, Naveen Valluri, et al. Biomedclip: a multimodal biomedical foundation model pretrained from fifteen million scientific image-text pairs. arXiv preprint arXiv:2303.00915, 2023a.

Xiaoman Zhang, Chaoyi Wu, Ziheng Zhao, Weixiong Lin, Ya Zhang, Yanfeng Wang, and Weidi Xie. Pmc-vqa: Visual instruction tuning for medical visual question answering. arXiv preprint arXiv:2305.10415, 2023b.

A EXPERIMENT

A.1 EXPERIMENTAL SETUP

A.1.1 DATA STATISTICS

The data quantities used in this study are presented in Table 6, Table 7 and Table 8. We clarify that for training the retriever, the data refers to the number of image-text pairs, while for fine-tuning, it refers to the number of QA items. The "All" category represents the total amount of data used to construct the preference dataset for RAG-PT. The training of RAG-PT includes three types of samples: (a) clean samples with originally correct answers that remain correct even after adding noise to the images, (b) clean image samples with originally incorrect answers that become correct, and (c) clean image samples with originally correct answers that become incorrect.

Table 6: Data statistics for medical VQA task. "Train (DR)" refers to the number of image-text pairs for retriever training, "All (RAG-PT)" refers to the total data for RAG-PT, and "Train (RAG-PT)-a/b/c" refer to the respective subsets for RAG-PT training.

Dataset	Train (DR)	All (RAG-PT)	Train (RAG-PT)-a	Train (RAG-PT)-b	Train (RAG-PT)-c
Ophthalomology	7000	3247	1082	1030	1135
Radiology	4034	4836	1612	1989	1235
Pathology	5000	1990	663	523	804

Table 7: Data statistics for report generation. "Train (DR)" refers to the number of image-text pairs for retriever training, "All (RAG-PT)" refers to the total data for RAG-PT, and "Train (RAG-PT)-a/b/c" refer to the respective sample categories for RAG-PT training.

Dataset	Train (R)	All (RAG-PT)	Train (RAG-PT)-a	Train (RAG-PT)-b	Train (RAG-PT)-c
Ophthalmology	7000	3247	142	78	207
Radiology	4034	4836	233	126	342

Table 8: Data statistics for various datasets. The rows represent the number of images and QA pairs for each dataset.

	Harvard-FairVLMed	IU-Xray	MIMIC-CXR	PMC-OA	Quilt-1M
# Images	713	589	700	530	559
# QA Items	4285	2573	3470	3124	1994

A.1.2 HYPERPARAMETER SETTINGS

Following the settings of CLIP (Radford et al., 2021), we adopt the same architecture and hyperparameters for the vision and text encoders. The vision encoder is a ResNet-50 (He et al., 2016), and the text encoder is a bio-bert-based model (Alsentzer et al., 2019). We use the AdamW optimizer with a learning rate of 10^{-4} and a batch size of 512. The model is trained for 360 epochs. For the first phase, we trained for 3 epochs, and for the second phase, the training was conducted for 1 epoch. Training for 20 hours on one A100 80G GPU. For the RAG-PT phase, we adjust the diffusion noise level, symbolized by ξ through a specific formula: $\xi = \text{Sigmoid}(l_t) \times (0.5 \times 10^{-2} - 10^{-5}) + 10^{-5}$, where ϵ is drawn from a normal distribution. The reports available for retrieval are from the training set of the corresponding dataset. In our experiments, we apply cross-validation to tune all hyperparameters with grid search. All the experiments are implemented on PyTorch 2.1.2 using four NVIDIA RTX A6000 GPUs. It takes roughly 3 and 4 hours for fine-tuning CLIP and LLaVA-Med-1.5 7B, respectively.

A.2 EVALUATED DATASETS

We utilize five open-source medical vision-language datasets, i.e., MIMIC-CXR (Johnson et al., 2019), IU-Xray (Demner-Fushman et al., 2016), Harvard-FairVLMed (Luo et al., 2024), PMC-OA (Lin et al., 2023a) and Quilt-1M (Ikezogwo et al., 2024).

- **MIMIC-CXR** (Johnson et al., 2019) is a large publicly available dataset of chest X-ray images in DICOM format with associated radiology reports.
- **IU-Xray** (Demner-Fushman et al., 2016) is a dataset that includes chest X-ray images and corresponding diagnostic reports.
- **Harvard-FairVLMed** (Luo et al., 2024) focuses on fairness in multimodal fundus images, containing image and text data from various sources. It aims to evaluate bias in AI models on this multimodal data comprising different demographics.
- **PMC-OA** (Lin et al., 2023a) is a large-scale dataset comprising figure-caption pairs extracted from PubMed Central. It covers 2,478,267 papers and includes a total of 12,211,907 figure-caption pairs. We only use the pathology subset filtered by GPT-4 based on the captions.
- **Quilt-1M** (Ikezogwo et al., 2024) is the largest vision-language dataset in histopathology, containing 1 million image-text pairs sourced from platforms such as YouTube, Twitter, research papers, and other parts of the internet.

A.3 Evaluated Models

We evaluate five open-source Med-LVLMs, *i.e.*, LLaVA-Med (Li et al., 2023a), Med-Flamingo (Moor et al., 2023), MedVInT (Zhang et al., 2023b), RadFM (Wu et al., 2023b), miniGPT-Med (Alkhaldi et al., 2024). The selected models are all at the 7B level.

- **LLaVA-Med** (Li et al., 2023a) is a vision-language conversational assistant, adapting the general-domain LLaVA (Liu et al., 2024b) model for the biomedical field. The model is fine-tuned using a novel curriculum learning method, which includes two stages: aligning biomedical vocabulary with figure-caption pairs and mastering open-ended conversational semantics. It demonstrates excellent multimodal conversational capabilities.
- **Med-Flamingo** (Moor et al., 2023) is a multimodal few-shot learner designed for the medical domain. It builds upon the OpenFlamingo, continuing pre-training with medical image-text data from publications and textbooks. This model aims to facilitate few-shot generative medical visual question answering, enhancing clinical applications by generating relevant responses and rationales from minimal data inputs.
- **RadFM** (Wu et al., 2023b) serve as a versatile generalist model in radiology, distinguished by its capability to adeptly process both 2D and 3D medical scans for a wide array of clinical tasks. It integrates ViT as visual encoder and a perceiver module, alongside the MedLLaMA language model, to generate sophisticated medical insights for a variety of tasks. This design allows RadFM to not just recognize images but also to understand and generate human-like explanations.
- **MedVInT** (Zhang et al., 2023b), which stands for Medical Visual Instruction Tuning, is designed to interpret medical images by answering clinically relevant questions. This model features two variants to align visual and language understanding: MedVInT-TE and MedVInT-TD. Both MedVInT variants connect a pre-trained vision encoder ResNet-50 adopted from PMC-CLIP (Lin et al., 2023a), which processes visual information from images. It is an advanced model that leverages a novel approach to align visual and language understanding.
- **miniGPT-Med** (Alkhaldi et al., 2024) is a vision-language model derived from large-scale language models and tailored for radiology diagnosis applications. It handles various medical vision-language task using distinct task identifiers, demonstrating advanced performance in disease grounding, medical report generation, and medical VQA.

A.4 Overview of the Baselines

We compare MMed-RAG with two types of LVLM hallucination mitigation methods that show promising results in natural image understanding. 1) Decoding-based methods, including Greedy Decoding, Beam Search (Sutskever et al., 2014), DoLa (Chuang et al., 2023), OPERA (Huang et al., 2023), VCD (Leng et al., 2023). These methods manipulate the logits of the model's output tokens to enhance factual accuracy. 2) Multimodal RAG-based methods, including MedDr (He et al., 2024), FactMM-RAG (Sun et al., 2024b), RULE (Xia et al., 2024b).

Instruction [Round1] You are a professional medical expert. I will provide you with some medical reports. Please generate some questions with answers (the answer should be yes or no) based on the provided report. The subject of the questions should be the medical image or patient, not the report. Below are the given report: [REPORT] **Instruction [Round2]** Please double-check the questions and answers, including how the questions are asked and whether the answers are correct. You should only generate the questions with answers and no other unnecessary information. Below are the given report and QA pairs in round1: [REPORT] [QA PAIRS R1]

Table 9: The instruction to GPT-4 for generating QA pairs.

- **Greedy decoding** involves selecting the most probable next token at each step of generation. While it is efficient and straightforward, it can lead to suboptimal outcomes by getting stuck in repetitive or less creative patterns.
- **Beam search** (Sutskever et al., 2014) expands on greedy decoding by maintaining multiple candidate sequences (or "beams") at each step, allowing for a broader exploration of possible outputs. This approach balances quality and diversity by selecting the top-k sequences based on their probabilities, resulting in more coherent and creative text generation compared to greedy decoding.
- **DoLa** (Chuang et al., 2023) derives the next-token distribution by contrasting the logits projected from later layers against those from earlier layers, leveraging the fact that factual knowledge in LLMs is typically localized within specific transformer layers.
- **OPERA** (Huang et al., 2023) is a LVLMs decoding method based on an Over-trust Penalty and a Retrospection-Allocation strategy The key insight is that hallucinations are closely tied to knowledge aggregation patterns in the self-attention matrix, where MLLMs tend to focus on summary tokens, neglecting image tokens and resulting in content hallucination.
- **VCD** (Leng et al., 2023) is a decoding method that tackles the object hallucination issue in LVLMs. It contrasts output distributions derived from original and distorted visual inputs to calibrate the model's output without the usage of external tools, reducing the the over-reliance on statistical bias and unimodal priors.
- **MedDr** (He et al., 2024) is a healthcare foundation model built upon generated diagnosis-based datasets, demonstrating advanced capabilities in various data modalities. Meddr also integrates a retrieval-augmented medical diagnosis strategy during inferencing to enhance factual accuracy.
- **FactMM-RAG** (Sun et al., 2024b) is a fact-aware multimodal retrieval-augmented pipeline for radiology report generation. It utilize RadGraph to annotate chest radiograph reports and mine clinically relevant pairs to train a universal multimodal retriever.
- **RULE** (Xia et al., 2024b) is an advanced medical retrieval-augmented generation strategy designed to enhance the factuality of Med-LVLMs. First, it introduces a robust strategy for controlling factuality risk through the calibrated selection of retrieved contexts. Second, RULE develops a preference optimization strategy to balance Med-LVLMs' intrinsic knowledge and the retrieved information.

A.5 Prompts

We convert the medical reports into a series of closed-ended questions with *yes* or *no* answers. To ensure the quality of the VQA data, we perform a round of self-checks using GPT-4 (OpenAI, 2023). Finally, we conduct an round of manual filtering to remove questions with obvious issues or those related to multiple images or patient histories. The prompt templates used are shown in Table 9.

A.6 Additional Results

A.6.1 Compatibility Analysis

To demonstrate the compatibility of our approach across different backbone models, we apply it to LLaVA-Med-1.0. As shown in Table 10, our method delivers an average improvement of 40.3% over the original LLaVA-Med-1.0, further highlighting its effectiveness in enhancing RAG performance and its adaptability to various backbones. MMed-RAG can be transferred to different Med-LVLMs, yielding consistent improvements across various domains, demonstrating the compatibility of our method.

Table 10: Performance on different backbones.

Model	IU-Xray		FairVLMed	
	VQA	RG	VQA	RG
LLaVA-Med-1.0	61.73	8.74	59.54	10.59
+MMed-RAG	**80.32**	**22.63**	**78.49**	**15.88**

A.6.2 Detailed Results of Other LVLMs

As shown in Table 11, we conduct a comparison of several general LVLMs and other Med-LVLMs, including GPT-4o (OpenAI, 2023), Gemini-1.5 (Reid et al., 2024), QwenVL (Bai et al., 2023), LLaVA-1.6 (Liu et al., 2024b), and InternVL-2 (Chen et al., 2024d). Our findings show that MMed-RAG consistently outperforms these models, further demonstrating its effectiveness.

Table 11: Accuracy (%) of different Med-LVLMs based on LLaVA-Med-1.5 on medical VQA task.

Models	**Radiology**		**Ophthalmology**	**Pathology**	
	IU-Xray	MIMIC-CXR	Harvard-FairVLMed	Quilt-1M	PMC-OA (Pathology)
LLaVA-Med-1.5	75.47	75.79	63.03	62.80	59.28
MMed-RAG	**89.54**	**83.57**	**87.94**	**72.95**	**64.54**
Med-Flamingo	26.74	61.27	42.06	27.11	32.62
MedVInT	73.34	66.06	35.92	26.81	27.77
RadFM	26.67	69.30	52.47	27.02	25.12
miniGPT-Med	54.87	53.92	66.73	26.82	27.03
GPT-4o	63.25	60.61	61.50	53.56	49.70
Gemini-1.5	59.73	61.02	58.53	56.88	52.17
LLaVA-v1.6	58.05	63.70	48.52	35.73	38.54
Qwen-VL-Chat	59.43	60.43	38.06	28.74	29.53
InternVL-2	54.06	59.47	44.38	37.82	34.40

A.6.3 Comparison with Domain-Specific Med-LVLMs and them with RAG-PT

We conduct experiments to compare our method with domain-specific Med-LVLMs as follows: Radiology: RadFM (Wu et al., 2023b), Pathology: Quilt-LLaVA (Seyfioglu et al., 2024), Ophthalmology: RetinaVLM (Holland et al., 2024). For radiology, we use the IU-Xray dataset to evaluate VQA. For pathology, we use the PMC-OA pathology subset to evaluate VQA. For ophthalmology, since the domain-specific Med-LVLM, i.e., RetinaVLM, is only trained on report-generation tasks, we use the Harvard-FairVLMed dataset to evaluate report generation. As shown in Table 12, our method significantly outperforms each domain-specific Med-LVLM. Additionally, we apply RAG-PT to each domain-specific Med-LVLM. As shown in Table 12, after incorporating RAG-PT, the performance of these models improve significantly, demonstrating the compatibility of our method. Furthermore, domain-specific Med-LVLMs could outperform generalist Med-LVLMs in their specialized domains, as they are fine-tuned using specialized medical domain data. While this significantly enhances their medical understanding in specific domains, it may reduce their generalization ability, such as their capacity to comprehend retrieved information. Consequently, even after incorporating RAG-PT, the performance of several domain-specific Med-LVLMs (e.g., RetinaVLM and RadFM) is inferior to MMed-RAG.

Table 12: Model performance comparison with domain-specific Med-LVLMs.

Model	Radiology			Pathology			Ophthalmology		
	Acc	F1	AUC	Acc	F1	AUC	BLEU	ROUGE-L	METEOR
RadFM	26.67	30.36	55.31	-	-	-	-	-	-
+ RAG-PT	48.39	39.40	59.70	-	-	-	-	-	-
Quilt-LLaVA	-	-	-	62.59	72.30	56.96	-	-	-
+ RAG-PT	-	-	-	**64.72**	**73.36**	61.39	-	-	-
RetinaVLM	-	-	-	-	-	-	19.96	12.73	13.52
+ RAG-PT	-	-	-	-	-	-	22.26	14.64	16.87
LLaVA-Med-1.5	75.47	64.04	67.46	59.28	71.98	54.19	18.11	11.36	10.75
MMed-RAG	**84.10**	**71.92**	86.40	64.54	73.09	**61.42**	**24.82**	**16.59**	**19.85**

A.6.4 Results on Other Domain

We apply RAG-PT to one additional domain (i.e., environmental ecosystems modeling) to further validate the effectiveness of RAG-PT. We conduct experiments on two environmental system modeling datasets (Li et al., 2024a). The CRW-Temp dataset is a river water temperature prediction dataset aimed at forecasting the daily average water temperature of a specific day based on observed physical variables. The CRW-Flow dataset focuses on predicting river segment flow based on observed physical variables. The model used is LITE (Li et al., 2024a), an environmental system large model based on LLaMA2 (Touvron et al., 2023). We train a semantic time-series encoder using time-series information-text pairs, which works in conjunction with a text encoder as the retriever. Then we retrieve the most similar environmental descriptions based on the current environmental descriptions. As shown in Table 13, our approach demonstrates significant performance improvements on tasks in this domain.

Table 13: Performance comparison of different models on CRW-Temp and CRW-Flow datasets.

Model	CRW-Temp		CRW-Flow	
	RMSE	MAE	RMSE	MAE
LITE (Li et al., 2024a)	2.02	1.70	2.39	1.02
+RAG	1.93	1.62	2.27	0.96
+RAG-PT	**1.74**	**1.46**	**2.11**	**0.90**

A.6.5 Statistics of Copy-Reference Rate and Over-Reliance Rate for more LVLMs.

Following the alignment analysis method we apply to LLaVA-Med-1.5 in Section 3.3, we conduct two alignment analysis tests on multiple open-source Med-LVLMs and commercial LVLMs using the Harvard-FairVLMed dataset with the incorporation of retrieved information. These tests respectively evaluate (1) cross-modality alignment and (2) overall alignment with the ground truth. As shown in Table 14, the results indicate that both existing open-source Med-LVLMs and commercial LVLMs exhibit misalignment issues with retrieved information. In addition, it is worthwhile to mention that GPT-4o demonstrates the best alignment performance compared with other models when incorporating RAG, especially in cross-modal alignment. This is likely because GPT-4o has been well-trained in visual perception and may also have utilized some post-training methods (like preference optimization) to optimize modal alignment.

A.6.6 Detailed Ablation Analysis

Preference data designed for different alignment objectives can indeed produce varying effects. Therefore, conducting ablation experiments on combinations of different types of preference data is necessary. We perform comprehensive ablation experiments on RAG-PT 1/2/3 as well as their combinations (RAG-PT 1+2, 2+3, 1+3) to analyze the effectiveness of each type of data and their combinations. We find that the combination of 1+3 produced the most significant results, indicating that the two misalignment issues (i.e., cross-modality and over-reliance issues) are the most

Table 14: Comparison of Copy-Reference Rate and Over-Reliance Rate across different models.

Model	Copy-Reference Rate	Over-Reliance Rate
LLaVA-Med-1.5	55.08	43.31
Med-Flamingo	60.17	33.74
miniGPT-Med	56.75	46.06
GPT-4o	12.54	24.80

prominent. Targeted mitigation of these two issues yielded the greatest improvement. However, incorporating data for all three alignment objectives yields the best performance, demonstrating the importance of each alignment component.

Table 15: Ablation results using RAG-PT based on subsets of preference data.

Model	IU-Xray		Harvard-FairVLMed	
	VQA	RG	VQA	RG
LLaVA-Med-1.5	68.99	10.04	66.63	13.41
+RAG-PT 1	80.19	19.38	79.42	18.37
+RAG-PT 2	80.27	20.16	79.35	18.66
+RAG-PT 3	81.30	19.43	80.07	18.92
+RAG-PT 1+2	82.58	22.74	82.08	18.97
+RAG-PT 1+3	82.96	24.50	82.87	19.22
+RAG-PT 2+3	83.61	25.77	83.89	19.30
+RAG-PT 1+2+3	**85.58**	**29.69**	**87.02**	**20.31**

A.6.7 External Validation

Considering the risk of overfitting, we use external validation datasets from the same domain to evaluate the generalizability of MMed-RAG. We select two domain-specific subsets from PubMed-Vision (Chen et al., 2024b), i.e., fundus digital photography and microscopy image, for ophthalmology and pathology, respectively. The results show that MMed-RAG still significantly outperforms other Med-LVLMs on the external validation datasets, indicating MMed-RAG performs well when generalized to external datasets, demonstrating its strong generalization capability.

Table 16: Performance comparison of models on external validation datasets.

Model	Ophthalmology			Pathology		
	BLEU	ROUGE-L	METEOR	Acc	F1	AUC
LLAVA-Med-1.5	17.11	20.05	17.09	59.65	71.90	54.87
MMed-RAG	22.64	14.98	17.85	62.88	72.24	59.69

A.6.8 Detailed BLEU Score

We report the average BLEU score above. Detailed results are provided in Table 17.

A.6.9 Deeper Analysis of Retriever

We have tried training a general retriever by mixing images from all modalities together, instead of using a domain-specific retriever. We conduct experiments based on BiomedCLIP and MedCLIP, but the results are unsatisfactory. Then we adopt an MoE (Mixture of Experts) architecture (Shazeer et al., 2017; Riquelme et al., 2021). Based on CLIP-MoE, we fine-tune CLIP-MoE (Zhang et al., 2024) with mixing images from all medical imaging modalities, but the performance is still suboptimal. This might be because CLIP-MoE is not pretrained on large-scale biomedical data. All the results are reported in Table 18. Considering model performance, we ultimately adopt a domain-specific retriever architecture. In fact, this approach is both flexible and scalable. Similar to a general retriever, encountering a completely new modality may still require retraining the retriever

Table 17: BLEU Score (%) of different methods based on LLaVA-Med-1.5 on report generation task.

Models	Radiology								Ophthalmology			
	IU-Xray				MIMIC-CXR				Harvard-FairVLMed			
	BLEU-1	BLEU-2	BLEU-3	BLEU-4	BLEU-1	BLEU-2	BLEU-3	BLEU-4	BLEU-1	BLEU-2	BLEU-3	BLEU-4
LLaVA-Med-1.5	17.69	10.55	6.47	3.83	21.82	13.35	6.11	3.64	32.57	19.86	9.11	5.38
+ Greedy	21.04	12.57	5.75	3.35	29.91	18.26	8.27	5.03	32.40	19.82	9.04	5.37
+ Beam Search	21.78	12.71	6.05	3.63	30.55	17.79	8.49	5.09	33.07	19.14	9.14	5.48
+ DoLa	21.22	12.39	5.90	3.54	30.80	17.97	8.58	5.15	32.87	19.02	9.08	5.45
+ OPERA	19.79	11.19	5.33	3.20	27.72	16.05	7.65	4.59	29.90	17.45	8.32	4.99
+ VCD	19.35	10.94	5.21	3.13	27.27	15.76	7.51	4.51	30.14	17.61	8.39	5.04
+ MedDr	22.27	12.99	6.19	3.71	33.43	19.33	9.22	5.53	35.64	20.61	9.82	5.89
+ FactMM-RAG	26.45	15.25	7.26	4.36	33.64	19.44	9.27	5.56	37.47	21.64	10.30	6.18
+ RULE	49.56	28.61	13.62	8.17	33.47	19.36	9.23	5.54	40.21	23.26	11.08	6.66
MMed-RAG	56.48	32.67	15.56	9.34	41.81	24.18	11.52	6.92	44.65	25.79	12.29	7.38

to achieve good retrieval performance, which incurs additional costs. For mixed datasets, as the number of modalities increases, training a general retriever becomes increasingly challenging, making it difficult to achieve reliable retrieval within a single domain. We address this by using a domain identification module to classify the input image by modality and select the corresponding retriever. In the future, a potential solution could involve pretraining a general retriever on large-scale biomedical data using a Mixture of Experts (MoE) architecture to explore whether it is possible to develop a general retriever.

Table 18: Performance comparison based on different retrievers.

Model	IU-Xray		
	Acc	F1	AUC
LLaVA-Med	75.47	64.04	67.46
+ RAG (BiomedCLIP-FT)	79.09	65.87	69.52
+ RAG (MedCLIP-FT)	75.13	63.88	67.16
+ RAG (CLIP-MoE-FT)	72.13	62.72	65.11
+ RAG (Ours)	84.82	68.85	77.54

A.6.10 Comparison under Few-Shot Setting

All our experiments are conducted under a zero-shot setting. We conduct experiments on LLaVA-Med-1.5 using the same few-shot strategy as in Med-Flamingo. The results show that compared to the zero-shot setting, the model's performance significantly decreases, even with RAG applied. Our analysis of this phenomenon reveals that, unlike Med-Flamingo, LLaVA-Med does not use interleaved multimodal data for pretraining. As a result, it lacks the capability for few-shot learning. This point has been mentioned in some discussion forums and GitHub issues. In addition, LLaVA-1.5's unsatisfactory performance on multi-image understanding benchmarks also supports this observation (Wang et al., 2024; Meng et al., 2024).

Table 19: Performance comparison under zero-shot and few-shot settings.

Model	IU-Xray		
	Acc	F1	AUC
LLaVA-Med (zero-shot)	75.47	64.04	67.46
+MMed-RAG	89.54	80.72	87.13
LLAVA-Med (few-shot)	66.77	51.56	66.60
+MMed-RAG	84.10	71.92	86.40

A.6.11 Performance Comparison of the Retriever

Regarding the retriever's performance, as shown in Table 20, we compared the performance of our retriever with several CLIP-based models on radiology datasets for image-to-text retrieval. The

results demonstrate that our retriever significantly outperforms the other models in retrieval performance.

Table 20: Performance comparison of different retrievers on Recall@1 (R@1) and Recall@5 (R@5) metrics.

Model	R@1	R@5
CLIP	3.91	7.88
PubMedCLIP	1.47	1.64
MedCLIP	6.74	12.69
BiomedCLIP	15.7	23.8
PMC-CLIP	12.3	21.2
Ours	45.6	71.8

A.6.12 RATIONALE-GUIDED RAG

For retrieved information, we minimize noise by optimizing the number of retrieved contexts k (e.g., Adaptive Retrieved Context Selection in Section 3.2). Following this, we introduce RAG-PT to specifically address the misalignment issues that arise after incorporating RAG, thereby strengthening Med-LVLM to balance its internal knowledge and external retrieval information. We employ a rationale-guided approach (Wei et al., 2024) that uses LLM to explicitly learn denoising of retrieved content through self-synthesized rationales. First, given a question, the retrieved documents, and the ground truth from the training set, we prompt a powerful Med-LLM (i.e., LLaMA3-Med42-70B (Christophe et al., 2024)) to generate a rationale. This rationale explains how to derive the answer from potentially noisy inputs. Next, we use the synthesized rationale from the previous step to guide another smaller Med-LLM (i.e., LLaMA3-Med42-7B (Christophe et al., 2024)) to explicitly learn denoising of the retrieved documents through in-context learning and supervised learning. By employing this rationale-guided Med-LLM to filter noisy retrieval information, the reliability of our retrieved data improves. Experimental results show that after rationale-guided RAG, the model's performance further improved.

Table 21: Performance comparison on IU-Xray dataset, including RAG and Rationale-Guided RAG variants.

Model	IU-Xray		
	Acc	F1	AUC
LLaVA-Med	75.47	64.04	67.46
+ RAG	84.82	68.85	77.54
+ RAG-PT	89.54	80.72	87.13
+ Rationale-Guided RAG	85.38	69.23	77.90
+ RAG-PT	89.91	80.86	87.32

A.7 THE CONTRIBUTION OF DOMAIN-SPECIFIC RETRIEVERS

We design a domain-specific retriever leveraging a generalist Med-LVLM to retrieve information from a dedicated database based on the identified modality of the input medical image. Here, the domain identification models used are capable of reliably recognizing modalities with high accuracy (99.83% accuracy in our experiments). For radiology VQA tasks, input radiology images are classified as "radiology" by the model, enabling the retrieval of knowledge exclusively from the radiology database to enhance generation. All retrieved documents are specific to radiology and exclude other modalities.

A.8 EXPLANATION OF CROSS-MODALITY ALIGNMENT

To construct preference pairs for cross-modality alignment, we first select a preferred response by having the model generate an answer using the correct medical image, clinical query, and retrieved

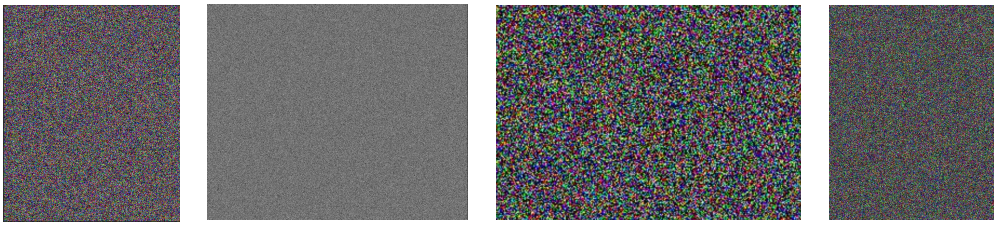

Figure 5: Illustration Examples for noisy images in cross-modality alignment.

knowledge, ensuring the response matches the ground-truth answer. Then, we select a dispreferred response by introducing an unrelated input image. This unrelated image is selected by finding the one with the lowest similarity to the target image and adding noise to distort it further. The dispreferred response is generated when the model uses this noisy, unrelated image along with the query and retrieved knowledge to still produce the correct answer. By comparing these pairs during training, the model learns to prioritize relevant and accurate inputs (e.g., the correct medical image) over noisy or irrelevant ones, improving cross-modality alignment.

A.9 Analysis of Noisy Image in Cross-Modality Alignment

In medical imaging, noise refers to random variations in image signals caused by hardware limitations or environmental factors (Gravel et al., 2004; Sanchez et al., 2012). However, the noise we refer to here pertains to images unrelated to the original image, generated through a two-step process: 1. We use a retriever to select images with the lowest similarity to the target image. 2. We introduce strong diffusion noise to these images. As a result, the noisy images in our case are almost entirely random noise and are not merely examples of domain shifts, such as changes in lighting conditions. Refer to the third section of Figure 1 for examples, and additional examples are included in the Figure 5 for reference.

The motivation behind our design is that replacing the original image with a highly noisy image while adding retrieved information corresponding to the original image reveals a significant issue of cross-modal misalignment in the Med-LVLM—namely, it ignores the image information and directly copies the retrieved contexts. To mitigate this issue, we construct such preference pairs to specifically strengthen the model's cross-modal alignment capability.

A.10 Explanation of Over Reliance Rate

The overall alignment issue arises from the conflict between retrieved information and the model's internal knowledge. For retrieved information, we cannot guarantee 100% accuracy, so some noise is inevitable. The Over-Reliance (OR) rate shown in Figure 3 refers to the proportion of initially correct responses that become incorrect after adding the retrieved context, calculated relative to the total number of incorrect samples, not the total number of all samples. This rate represents the proportion of errors caused by over-reliance, rather than indicating poor performance of the retriever. Through RAG-PT, we can effectively mitigate this issue, significantly reducing the OR rate.

B PROOFS FOR THEORETICAL RESULTS IN SECTION 4

Here we provide proofs for the results in Section 4.

B.1 NOTATIONS

Let x_v, y, x_t, x_r be input medical image, ground-truth answer, question, and retrieved information, respectively. Denote $(x_w, y_{w,o}) \sim q_p(x_w, y_{w,o}|x_t, x_r)$ and $(x_l, y_{l,o}) \sim q_l(x_l, y_{l,o}|x_t, x_r)$ as distributions of the preferred responses and dispreferred responses. Let x denote (x_v, x_r, x_t). We aim to a fine-tune a generative model $\pi_\theta(y|x, x_t)$ through DPO loss (Rafailov et al., 2023):

$$\arg\min_{\pi_\theta} \mathbb{E}_{(x_w, x_l, y_{w,o}, y_{l,o}) \sim \mathcal{D}} U\left(\alpha \log \frac{\pi_\theta(y_{w,o}|x)}{\pi_o(y_{w,o}|x)} - \alpha \log \frac{\pi_\theta(y_{l,o}|x)}{\pi_o(y_{l,o}|x)}\right). \tag{14}$$

where $U(t) = \log(1 + \exp(-t))$. Define the weight of x_v with respect to $\log \pi_\theta(y|x)$ as

$$\text{wt}(x_v, \pi_\theta) := \mathbb{E}_{y \sim \pi_\theta(\cdot|x)} \left[\frac{\partial}{\partial x_v} \log \pi_\theta(y|x)\right]^2 \tag{15}$$

B.2 ASSUMPTIONS

Assumption B.1 *(Large parameter space) Assume that $\pi(x_v, y|x_t, x_r)$ lies in the optimization space $\{\pi_\theta, \theta \in \Theta\}$ such that $\pi(x_v, y|x_t, x_r) \propto \pi_o(x_v, y|x_t, x_r) \left(\frac{q_w(x_v, y|x_t, x_r)}{q_l(x_v, y|x_t, x_r)}\right)^{\frac{1}{\alpha}}$*

Assumption B.1 requires that the parameter space sufficiently large to ensure that π_θ can achieve its global optimum, allowing us to represent the optimizer with a closed form.

Assumption B.2 *Let $h(x, y)$, abbreviate as h, be*

$$h := \left[\sum_y \pi_o(y|x) \left(\frac{q_w(y|x)}{q_l(y|x)}\right)^{\frac{1}{\alpha}}\right]^{-1} \left(\frac{q_w(y|x)}{q_l(y|x)}\right)^{\frac{1}{\alpha}} \tag{16}$$

Assume that wt$(x_v, \pi_o) < c^2$, where

$$c = \sqrt{\left\|\sqrt{\pi_o(y|x)} \cdot \frac{\partial}{\partial x_v} h\right\|_2^2 + \int \left(\frac{\partial}{\partial x_v} h\right)^2 \frac{\pi_o(y|x)}{h} dy} - \left\|\sqrt{\pi_o(y|x)} \cdot \frac{\partial}{\partial x_v} h\right\|_2 \tag{17}$$

Assumption B.3 *Let $h_1(x_v, x_t, x_r, y)$, abbreviate as h_1, be*

$$h_1 := \left[\sum_y \pi_o(y|x) \left(\frac{q_w^1(y|x_v, x_t, x_r) + q_w^2(y|x_v, x_t)}{q_l^1(y|x_v, x_t) + q_l^2(y|x_v, x_t, x_r)}\right)^{\frac{1}{\alpha}}\right]^{-1} \left(\frac{q_w^1(y|x_v, x_t, x_r) + q_w^2(y|x_v, x_t)}{q_l^1(y|x_v, x_t) + q_l^2(y|x_v, x_t, x_r)}\right)^{\frac{1}{\alpha}} \tag{18}$$

Assume that wt$(x_r, \pi_o) < c_1^2$ and wt$(\tilde{x}_r, \pi_o) > c_2^2$, where

$$\begin{aligned} c_1 &= \sqrt{\left\|\sqrt{\pi_o} \cdot \frac{\partial h_1}{\partial x_r}\right\|_2^2 + \int \left(\frac{\partial h_1}{\partial x_r}\right)^2 \frac{\pi_o}{h_1} dy} - \left\|\sqrt{\pi_o} \cdot \frac{\partial h_1}{\partial x_r}\right\|_2 \\ c_2 &= \sqrt{\left\|\sqrt{\pi_o} \cdot \frac{\partial h_1}{\partial \tilde{x}_r}\right\|_2^2 + \int \left(\frac{\partial h_1}{\partial \tilde{x}_r}\right)^2 \frac{\pi_o}{h_1} + \left(\frac{\partial \pi_o}{\partial \tilde{x}_r}\right)^2 \frac{h_1}{\pi_o} dy} + \left\|\sqrt{\pi_o} \cdot \frac{\partial h_1}{\partial \tilde{x}_r}\right\|_2 \end{aligned} \tag{19}$$

B.3 PROOFS

Lemma B.1 *Suppose that Assumption B.1 hold, optimizing equation 14 gives*

$$\pi_\theta(y|x) \propto \pi_o(y|x) \left(\frac{q_w(y|x)}{q_l(y|x)}\right)^{\frac{1}{\alpha}} \tag{20}$$

Lemma B.1 indicates that the model tends to increase $\pi_o(y|x)$ if $q_w(y|x) > q_l(y|x)$, which is more likely to occur when (x_v, y) represents a preferred sample given x_t and x_r. Below, we provide an application of Lemma B.1 using a linear regression example. Lemma B.1 is proved with Lemma B.2 and Lemma B.3.

Lemma B.2 *(Lemma C.1 in Chen et al. (2024e)) For $a, b > 0$, the following inequality holds*

$$a \cdot U(t) + b \cdot U(-t) \geq a \log(1 + b/a) + b \log(1 + a/b)$$

and equality holds if and only if $t = \log(a/b)$

Lemma B.3 *Denote*

$$\begin{cases} p_1(x_w, y_{w,o}, x_l, y_{l,o}|x_t, x_r) & = q_w(x_w, y_{w,o}|x_t, x_r) \cdot q_l(x_l, y_{l,o}|x_t, x_r) \\ p_2(x_w, y_{w,o}, x_l, y_{l,o}|x_t, x_r) & = q_l(x_w, y_{w,o}|x_t, x_r) \cdot q_w(x_l, y_{l,o}|x_t, x_r) \end{cases}$$

and abbreviated as p_1 and p_2 for notational convenience. Then,

$$\begin{aligned} &2\mathbb{E}_{\mathcal{D}}\left[U\left(f(x_w, y_{w,o}, x_t, x_r) - f(x_l, y_{l,o}, x_t, x_r)\right)\right] \\ \geq &2\log 2 - D_{\mathrm{KL}}\left(p_1 \middle\| \frac{p_1 + p_2}{2}\right) - D_{\mathrm{KL}}\left(p_2 \middle\| \frac{p_1 + p_2}{2}\right) \end{aligned} \tag{21}$$

Equality holds if and only if

$$f(x, y) = g(x) + \log \frac{q_w(x_v, y|x_t, x_r)}{q_l(x_v, y|x_t, x_r)} \tag{22}$$

where $g(x)$ is any function that is possibly dependent on x_v, x_t and x_r.

Proof B.1

$$\begin{aligned} &2\mathbb{E}_{\mathcal{D}}\left[U\left(f(x_w, y_{w,o}, x_t, x_r) - f(x_l, y_{l,o}, x_t, x_r)\right)\right] \\ =&\int q(x_t, x_r) \cdot p_1 \cdot U\left(f(x_w, y_{w,o}, x_t, x_r) - f(x_l, y_{l,o}, x_t, x_r)\right) dxdy \\ &+ \int q(x_t, x_r) \cdot p_2 \cdot U\left(f(x_l, y_{l,o}, x_t, x_r) - f(x_w, y_{w,o}, x_t, x_r)\right) dxdy \\ \geq &\int q(x_t, x_r)\left[p_1 \cdot \log\left(1 + \frac{p_2}{p_1}\right) + p_2 \cdot \log\left(1 + \frac{p_1}{p_2}\right)\right] dxdy \\ =&2\log 2 + \int q(x_t, x_r)\left[p_1 \cdot \log\left(\frac{p_1 + p_2}{2p_1}\right) + p_2 \cdot \log\left(\frac{p_1 + p_2}{2p_2}\right)\right] dxdy \\ =&2\log 2 - KL\left(p_1 \middle\| \frac{p_1 + p_2}{2}\right) - KL\left(p_2 \middle\| \frac{p_1 + p_2}{2}\right) \end{aligned} \tag{23}$$

where the first inequality follows from Lemma B.2. For equivalence,

$$f(x, y_{w,o}, x_t, x_r) - f(x_l, y_{l,o}, x_t, x_r) = \log \frac{q_w(x_w, y_{w,o}|x_t, x_r) \cdot q_l(x_l, y_{l,o}|x_t, x_r)}{q_l(x_w, y_{w,o}|x_t, x_r) \cdot q_w(x_l, y_{l,o}|x_t, x_r)} \tag{24}$$

Thus, for any $x_w, y_{w,o}, x_l, y_{l,o}, x_t, x_r$,

$$f(x_w, y_{w,o}, x_t, x_r) - \log \frac{q_w(x_w, y_{w,o}|x_t, x_r)}{q_l(x_w, y_{w,o}|x_t, x_r)} = f(x_l, y_{l,o}, x_t, x_r) - \log \frac{q_w(x_l, y_{l,o}|x_t, x_r)}{q_l(x_l, y_{l,o}|x_t, x_r)} \tag{25}$$

Therefore, equation 25 holds if and only if there exists some $g(x_v, x_t, x_r)$ such that

$$f(x_v, x_t, x_r, y) = g(x_t, x_r) + \log \frac{q_w(x_v, y|x_t, x_r)}{q_l(x_v, y|x_t, x_r)} \tag{26}$$

Lemma B.3 provides a closed-form solution to equation 14 if the parameter space is sufficiently large. This lemma is crucial for the proof Lemma B.1, which follows below

Proof B.2 *According to the Assumption B.1, we have*

$$\pi(x_v, y|x_t, x_r) = \hat{g}(x_t, x_r)\pi_o(x_v, y|x_t, x_r)\left(\frac{q_w(x_v, y|x_t, x_r)}{q_l(x_v, y|x_t, x_r)}\right)^{\frac{1}{\alpha}} \tag{27}$$

After reparameterization,

$$\alpha \log\left(\frac{\pi(x_v, y|x_t, x_r)}{\pi_o(x_v, y|x_t, x_r)}\right) = \alpha \log[\hat{g}(x_t, x_r)] + \log\frac{q_w(x_v, y|x_t, x_r)}{q_l(x_v, y|x_t, x_r)} \tag{28}$$

which is the global minimum of

$$\arg\min_f \mathbb{E}_{\mathcal{D}}\left[U\left(f(x_w, y_{w,o}, x_t, x_r) - f(x_l, y_{l,o}, x_t, x_r)\right)\right] \tag{29}$$

by Lemma B.3. Since $\pi(x_v, y|x_t, x_r) \in \{\pi_\theta, \theta \in \Theta\}$ lies in the optimization space, we have

$$\begin{aligned}&\min_f \mathbb{E}_{\mathcal{D}} U\left(f(x_w, y_{w,o}, x_t, x_r) - f(x_l, y_{l,o}, x_t, x_r)\right)\\ =&\min_{\pi_\theta} \mathbb{E}_{\mathcal{D}} U\left(\alpha \log\frac{\pi_\theta(y_{w,o}|x_w, x_t, x_r)}{\pi_o(y_{w,o}|x_w, x_t, x_r)} - \alpha\log\frac{\pi_\theta(y_{l,o}|x_l, x_t, x_r)}{\pi_o(y_{l,o}|x_l, x_t, x_r)}\right)\end{aligned} \tag{30}$$

and $\pi_\theta(x_v, y|x_t, x_r)$ is the optimizer of equation 30, which gives

$$\begin{aligned}&\alpha\log\left(\frac{\pi_\theta(x_v, y|x_t, x_r)}{\pi_o(x_v, y|x_t, x_r)}\right) = g(x_t, x_r) + \log\frac{q_w(x_v, y|x_t, x_r)}{q_l(x_v, y|x_t, x_r)}\\ \Longrightarrow&\pi_\theta(x_v, y|x_t, x_r) = \pi_o(x_v, y|x_t, x_r)\left(\frac{q_w(x_v, y|x_t, x_r)}{q_l(x_v, y|x_t, x_r)}\right)^{\frac{1}{\alpha}}\exp\left(\frac{1}{\alpha}g(x_t, x_r)\right)\end{aligned} \tag{31}$$

Then

$$\begin{aligned}\pi_\theta(y|x) = \frac{\pi_\theta(x_v, y|x_t, x_r)}{\pi_\theta(x|x_t, x_r)} &= \frac{\pi_o(x_v, y|x_t, x_r)\left(\frac{q_w(x_v, y|x_t, x_r)}{q_l(x_v, y|x_t, x_r)}\right)^{\frac{1}{\alpha}}\exp\left(\frac{1}{\alpha}(g(x_t, x_r))\right.}{\sum_y \pi_o(x_v, y|x_t, x_r)\left(\frac{q_w(x_v, y|x_t, x_r)}{q_l(x_v, y|x_t, x_r)}\right)^{\frac{1}{\alpha}}\exp\left(\frac{1}{\alpha}(g(x_t, x_r))\right.}\\ &= \frac{\pi_o(y|x)\left(\frac{q_w(x_v, y|x_t, x_r)}{q_l(x_v, y|x_t, x_r)}\right)^{\frac{1}{\alpha}}}{\sum_y \pi_o(y|x)\left(\frac{q_w(x_v, y|x_t, x_r)}{q_l(x_v, y|x_t, x_r)}\right)^{\frac{1}{\alpha}}} = \frac{\pi_o(y|x)\left(\frac{q_w(y|x_v, x_t, x_r)}{q_l(y|x_v, x_t, x_r)}\right)^{\frac{1}{\alpha}}}{\sum_y \pi_o(y|x)\left(\frac{q_w(y|x_v, x_t, x_r)}{q_l(y|x_v, x_t, x_r)}\right)^{\frac{1}{\alpha}}}\end{aligned} \tag{32}$$

Corollary B.1 *Suppose that preferred responses (x_w, y_w) and dispreferred responses (x_l, y_l) satisfy $y_w = \beta x_w + \epsilon_1$ and $y_l = \tilde{\beta} x_l + \epsilon_2$ respectively. DPO for $y = \theta x_v + \epsilon_3$ is based on reference model $y = \theta_o x_v + \epsilon_4$, where ϵ_i's are independent and follow standard normal distribution. Then,*

$$\theta = \theta_o + \frac{1}{\alpha}(\beta - \tilde{\beta}) \tag{33}$$

Corollary B.1 is a direct application of Lemma B.1, indicating that the model updates coefficient θ_o towards the direction of β for preferred responses and away from $\tilde{\beta}$ for dispreferred responses.

Proof B.3 *Let $\phi(\cdot)$ denote the probability density function of standard normal, by Lemma B.1,*

$$\begin{aligned}&\phi(y - \theta x) \propto \phi(y - \theta_o x)\left(\frac{\phi(y - \beta x)}{\phi(y - \tilde{\beta} x)}\right)^{\frac{1}{\alpha}}\\ \Longrightarrow&\exp\left(\frac{1}{2}y^2 - \theta_1 xy\right) \propto \exp\left(\frac{1}{2}y^2 - \theta_o xy\right)\cdot\exp\left(-\frac{1}{\alpha}(\beta - \tilde{\beta})xy\right)\\ \Longrightarrow&\exp(\theta_1 xy) \propto \exp(\theta_o xy)\cdot\exp\left(\frac{1}{\alpha}(\beta - \tilde{\beta})xy\right)\\ \Longrightarrow&\theta = \theta_o + \frac{1}{\alpha}(\beta - \tilde{\beta})\end{aligned} \tag{34}$$

Lemma B.4 *For linear model $y = \theta_1 x_v + \theta_2 x_t + \epsilon$ such that $\epsilon \sim N(0,1)$, $wt(x_v, \pi_\theta) = \theta_1^2$*

Proof B.4 *Let $\phi(\cdot)$ denote the probability density function of standard normal,*

$$\begin{aligned} wt(x_v, \pi_\theta) &= \int \left(-\frac{1}{2} \frac{\partial}{\partial x_v} \left(y - \theta_1 x_v - \theta_2 x_t \right)^2 \right)^2 \phi(y - \theta_1 x_v - \theta_2 x_t) dy \\ &= \theta_1^2 \int \left(y - \theta_1 x_v - \theta_2 x_t \right)^2 \phi(y - \theta_1 x_v - \theta_2 x_t) dy \\ &= \theta_1^2 \int \left(\theta_1 x_v + \theta_2 x_t - y \right) \frac{d\phi(y - \theta_1 x_v - \theta_2 x_t)}{dy} dy \\ &= \theta_1^2 \int \phi(y - \theta_1 x_v - \theta_2 x_t) dy = \theta_1^2 \end{aligned} \tag{35}$$

Theorem B.2 *Suppose that Assumption B.2 holds, then cross-modality increase the weight of x_v.*

$$wt(x_v, \pi_\theta) > wt(x_v, \pi_o) \tag{36}$$

Proof B.5 *By Lemma B.1, we have*

$$\pi_\theta(y|x) = \pi_o(y|x) \cdot h(x,y), \quad \int \pi_o(y|x) \cdot h(x,y) dy = 1 \tag{37}$$

Abbreviate $h(x,y)$ and $\pi_o(y|x_v, x_t)$ as h and π_o respectively, we have

$$\begin{aligned} wt(x_v, \pi_\theta) - wt(x_v, \pi_o) &\geq \int \left(\frac{\frac{\partial}{\partial x_v} \pi_o}{\pi_o} + \frac{\frac{\partial}{\partial x_v} h}{h} \right)^2 \pi_o h \, dy - wt(x_v, \pi_o) \\ &\geq \int \left[\frac{\partial}{\partial x_v} h \right]^2 \frac{\pi_o}{h} dy - 2\sqrt{wt(x_v, \pi_o)} \cdot \left\| \sqrt{\pi_o} \cdot \frac{\partial}{\partial x_v} h \right\|_2 - wt(x_v, \pi_o) \end{aligned} \tag{38}$$

the second inequality follows from Cauchy–Schwarz inequality

$$\int \frac{\partial}{\partial x_v} \pi_o \cdot \frac{\partial}{\partial x_v} h \, dy = \int \frac{\partial}{\partial x_v} \pi_o \cdot \frac{\sqrt{\pi_o}}{\sqrt{\pi_o}} \cdot \frac{\partial}{\partial x_v} h \, dy \leq \sqrt{wt(x_v, \pi_o)} \cdot \left\| \sqrt{\pi_o} \cdot \frac{\partial}{\partial x_v} h \right\|_2 \tag{39}$$

Denote c as

$$c := \sqrt{\left\| \sqrt{\pi_o} \cdot \frac{\partial}{\partial x_v} h \right\|_2^2 + \int \left(\frac{\partial}{\partial x_v} h \right)^2 \frac{\pi_o}{h} dy} - \left\| \sqrt{\pi_o} \cdot \frac{\partial}{\partial x_v} h \right\|_2 \tag{40}$$

the last term in equation 38 is equivalent to

$$\left(c - \sqrt{wt(x_v, \pi_o)} \right) \cdot \left(\sqrt{wt(x_v, \pi_o)} + c + 2 \left\| \sqrt{\pi_o} \cdot \frac{\partial}{\partial x_v} h \right\|_2 \right) \tag{41}$$

Thus, $wt(x_v, \pi_\theta) > wt(x_v, \pi_o)$ if $\sqrt{wt(x_v, \pi_o)} < c$.

Theorem B.3 *Suppose that Assumption B.3 holds, the overall loss increase the weight of x_r and decrease the weight of $\tilde{x}_r$.*

$$wt(x_r, \pi_\theta) > wt(x_r, \pi_o), \quad wt(\tilde{x}_r, \pi_\theta) < wt(\tilde{x}_r, \pi_o) \tag{42}$$

Proof B.6 *The distribution of preferred responses can be considered as a mixture distribution: $q_w^1(x_v, y_{w,o}|x_t, x_r) + q_w^2(x_v, y_{w,o}|x_t)$. Similarly, for dispreferred responses, the distribution is represented as $q_l^1(x_v, y_{l,o}|x_t) + q_l^2(x_v, y_{l,o}|x_t, x_r)$. By Lemma B.1,*

$$\pi_\theta(y|x) = \pi_o(y|x) \cdot h_1(x,y), \quad \int \pi_o(y|x) \cdot h_1(x,y) dy = 1 \tag{43}$$

Abbreviate $h_1(x, y)$ as h_1. Follow the same procedure in the proof of Theorem B.2,

$$\begin{aligned} wt(x_r, \pi_\theta) - wt(x_r, \pi_o) &\geq \int \left[\frac{\partial}{\partial x_r} h_1\right]^2 \frac{\pi_o}{h_1} dy - 2\sqrt{wt(x_r, \pi_o)} \cdot \left\| \sqrt{\pi_o} \cdot \frac{\partial}{\partial x_r} h_1 \right\|_2 - wt(x_r, \pi_o) \\ &= \left(c_1 - \sqrt{wt(x_r, \pi_o)}\right) \cdot \left(\sqrt{wt(x_r, \pi_o)} + c_1 + 2\left\| \sqrt{\pi_o} \cdot \frac{\partial}{\partial x_r} h_1 \right\|_2\right) \end{aligned} \tag{44}$$

where we apply Cauchy–Schwarz inequality in equation 44.

$$c_1 = \sqrt{\left\| \sqrt{\pi_o(y|x)} \cdot \frac{\partial}{\partial x_r} h_1 \right\|_2^2 + \int \left(\frac{\partial}{\partial x_r} h_1\right)^2 \frac{\pi_o(y|x)}{h_1} dy} - \left\| \sqrt{\pi_o(y|x)} \cdot \frac{\partial}{\partial x_r} h_1 \right\|_2 \tag{45}$$

Thus, $wt(x_r, \pi_\theta) > wt(x_r, \pi_o)$ if $\sqrt{wt(x_r, \pi_o)} < c_1$. Again, by Cauchy–Schwarz inequality

$$\begin{aligned} & wt(\tilde{x}_r, \pi_\theta) - wt(\tilde{x}_r, \pi_o) \\ \leq & \int \left(\frac{\partial h_1}{\partial \tilde{x}_r}\right)^2 \frac{\pi_o}{h_1} + \left(\frac{\partial \pi_o}{\partial \tilde{x}_r}\right)^2 \frac{h_1}{\pi_o} dy + 2\sqrt{wt(\tilde{x_r}, \pi_o)} \cdot \left\| \sqrt{\pi_o} \cdot \frac{\partial h_1}{\partial \tilde{x}_r} \right\|_2 - wt(\tilde{x}_r, \pi_o) \\ = & -\left(\sqrt{wt(\tilde{x_r}, \pi_o)} - c_2\right) \cdot \left(\sqrt{wt(\tilde{x_r}, \pi_o)} - c_2 + 2\left\| \sqrt{\pi_o} \cdot \frac{\partial}{\partial \tilde{x}_r} h_1 \right\|_2\right) \end{aligned} \tag{46}$$

where

$$c_2 = \sqrt{\left\| \sqrt{\pi_o} \cdot \frac{\partial}{\partial \tilde{x}_r} h_1 \right\|_2^2 + \int \left(\frac{\partial}{\partial \tilde{x}_r} h_1\right)^2 \frac{\pi_o}{h_1} + \left(\frac{\partial}{\partial \tilde{x}_r} \pi_o\right)^2 \frac{h_1}{\pi_o} dy} + \left\| \sqrt{\pi_o} \cdot \frac{\partial}{\partial \tilde{x}_r} h_1 \right\|_2 \tag{47}$$

Thus, $wt(x_r, \pi_\theta) < wt(x_r, \pi_o)$ if $\sqrt{wt(x_r, \pi_o)} > c_2$.